Lithium Recovery from Hydraulic Fracturing Flowback and Produced Water using a Manganese-Based Sorbent

by

Adam John Seip

A thesis submitted in partial fulfillment of the requirements for the degree of

Master of Science

Department of Earth and Atmospheric Sciences

University of Alberta

Abstract

Increased demand for lithium products for use in lithium ion batteries has led to a search for new lithium resources in recent years in order to meet projected future consumption. One such potential lithium resource is low lithium bearing brines that are discharged from hydraulically fractured oil and gas wells as flowback and produced water (FPW). In this way, hydraulic fracturing presents an opportunity to turn what is normally considered a wastewater into a lithium resource. In this research, two manganese-based adsorbents that are selective toward lithium were prepared using a co-precipitation method and were employed for lithium recovery from FPW. At optimized conditions, lithium uptake reached 18 mg g^{-1}, with a > 80% lithium recovery within 30 minutes. The recovered lithium was isolated and concentrated to 15 mM in an acidic final product. The degree of sorbent loss during acid desorption of lithium were significantly higher for sorbents used to recover lithium from FPW as compared to recovery from a synthetic lithium-bearing brine (4.5% versus 0.8%); here, I propose that organic molecules present in the FPW reduce manganese in the sorbent structure during lithium sorption, leading to increased sorbent loss through reductive dissolution. Systematic characterization including wet chemical manganese valence measurements along with EXAFS and XPS show that tetravalent manganese in the sorbent is reduced during lithium sorption, and subsequently dissolves during acid desorption. Partial removal of these organic molecules by nanofiltration leads to decreased sorbent dissolution in acid. I show that dissolved organic molecules represent a critical control on the reductive dissolution of manganese-based lithium ion exchange sorbents.

Acknowledgements

I would like to thank, first and foremost, my supervisor Dr. Daniel Alessi, for giving me the opportunity to work on an extremely interesting project and for giving me great support, advice and direction along the way. I would also like to thank Dr. Salman Safari, who worked with me very closely on this project, and who gave me plenty of guidance throughout every aspect of my time at the University of Alberta.

I would like to acknowledge the funding sources which helped to finance this project, including the Natural Sciences and Engineering Research Council of Canada (NSERC) for the award of a Canada Graduate Scholarship – Master's (CGS-M), Discovery Grant to DSA (RGPIN-04134), a NSERC Collaborative Research and Development (CRD) grant to DSA (CRDPJ-519916), and support from E3 Metals Corporation.

Additionally, I would like to thank every person who helped me to perform the analyses required to complete this project, including Jonathan Banks, the people at the Advanced Water Research Lab, Carmen A. Velasco and Dr. Jose M. Cerrato at the University of New Mexico, and the people at the Diamond Light Source (especially Dr. Alan Chadwick and Dr. David Pickup) for the award of beam time as part of the Energy Materials Block Allocation Group SP14239.

Lastly, I would like to express thanks to every person who I worked alongside in the Alessi lab, along with my family and friends, who gave me plenty of encouragement and support throughout this entire process.

Table of Contents

List of Tables

List of Figures

1. Introduction

1.1. Lithium Uses and Global Demand

Lithium is a valuable resource which has been gaining public interest in recent years due to the expansion of the lithium battery market, primarily for use in electric vehicles.[1-3] Lithium is used in various industrial products including ceramics, glass, greases and lubricants, however the battery industry is emerging as the most significant contributor to global lithium demand.[4] In 2019, the battery industry accounted for 65% of lithium demand globally,[5] up from 46% only 2 years before.[6] This is not due to a shift in lithium usage; lithium use in batteries has given cause for a massive growth in lithium production. Global lithium production increased by an estimated 113% between 2016 and 2018,[4] with a total 2018 production of 85,000 tons of lithium.[4] Between the years 2003 and 2013, the lithium usage from rechargeable batteries increased by an average of 25% per year;[2] it is anticipated that this trend will continue, and that even with the global increase in lithium production, lithium availability may become the rate limiting factor in lithium battery production in the future.[7]

Currently, almost all of the lithium products used in industry in North America are imported from other countries;[8] for this reason, lithium supply security has become a priority for technology companies in North America.[4] A lithium production industry sourced from reserves in Western Canada could prove to be a profitable industry in Canada, could help to address the North American lithium supply security issue, and could contribute to the diversification of Alberta's economy.

1.2. Global Lithium Resources and Reserves

Lithium is a relatively abundant element in the lithosphere. By far the world's largest source of lithium is represented by the oceans; an estimated 230 to 250 billion tons of lithium exists in the world's oceans, however, because of its low concentration of 0.17 mg L^{-1} it is not normally considered to be commercially viable to recover.[9] A recent estimate of worldwide lithium resources (identified concentrations of lithium which may be potentially feasible to recover economically)[10] totaled 80 million tons.[5] Not all of these lithium resources, however, are considered to be reserves (the economically extractable fraction of a resource at present).[10] For this reason, current estimates of total global lithium reserves total 17 million tons.[5]

Lithium reserves exist as both mineral and brine deposits. Lithium production from brine sources is generally considered to require lower capital costs;[9] this lower cost is a contributor to the fact that approximately 87% of current global lithium reserves exist as brine deposits, while only 13% exist as mineral despoits.[9]

Chile and Australia are currently estimated to have the largest lithium reserves, with 8.6 million tons in the form of brine deposits, and 2.8 million tons, largely in the form of mineral deposits, respectively.[5] The largest lithium resources worldwide, however, are in Bolivia and Argentina, with 21 million and 17 million tons of lithium, respectively.[5] As demand for lithium rises and as lithium recovery technologies are further studied, many of these lithium deposits currently listed as resources may become economically extractable reserves in the future.

1.3. Lithium in Alberta

Canada has a considerable lithium resource, estimated at 2 million tons.[4,9] Of this resource, approximately 515,000 tons of lithium exists in the Leduc and Beaverhill Lake formation waters in west-central Alberta over an area of 4000 square kilometres.[10] The most significant lithium resource in Alberta lies in the Fox Creek area, which contains the highest concentration of high lithium bearing (> 75 ppm) formation water in Alberta, with some lithium concentrations reaching as high as 140 ppm (Figure 1a).[11] The cause of this lithium anomaly is unknown, however one hypothesis involves the mobilization of silicate-bearing fluids from the lithium containing magmatic basement rock to the aquifer via hydrothermal volcanic activity (Figure 1b).[11] This lithium resource exists at depths of 2500 – 3900 metres below the ground surface,[11] making traditional access to it a challenge; however, these lithium-bearing formation waters are associated with producing oil and gas wells in the Fox Creek area,[11] and therefore return to the surface as a byproduct of processes such as hydraulic fracturing.[12] Consequently, hydraulic fracturing flowback and produced water (FPW) from shale gas production wells represents an opportunity for lithium recovery,[13,14] which may prove to be a profitable industry in Alberta.

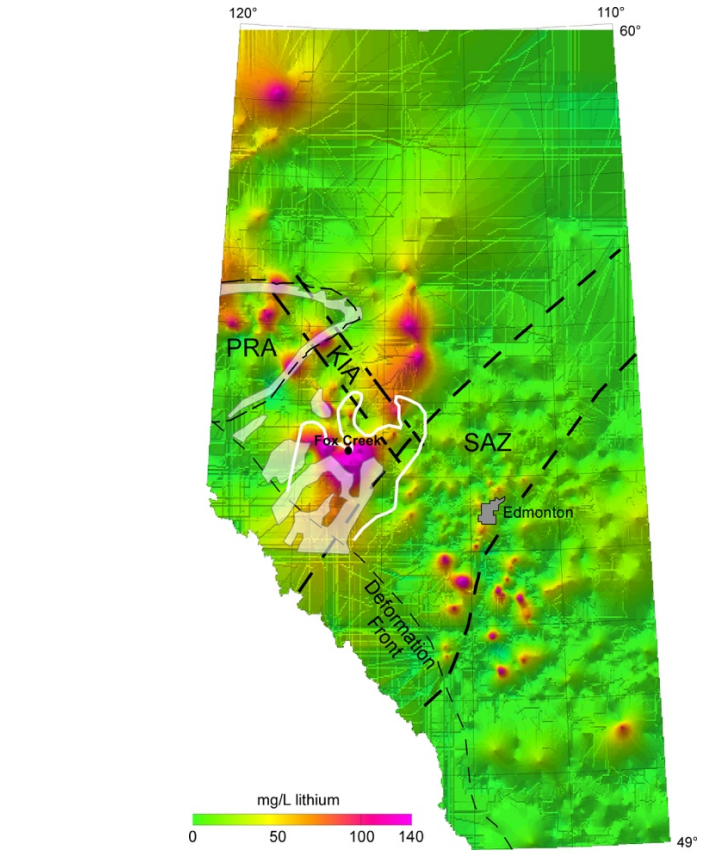

(a)

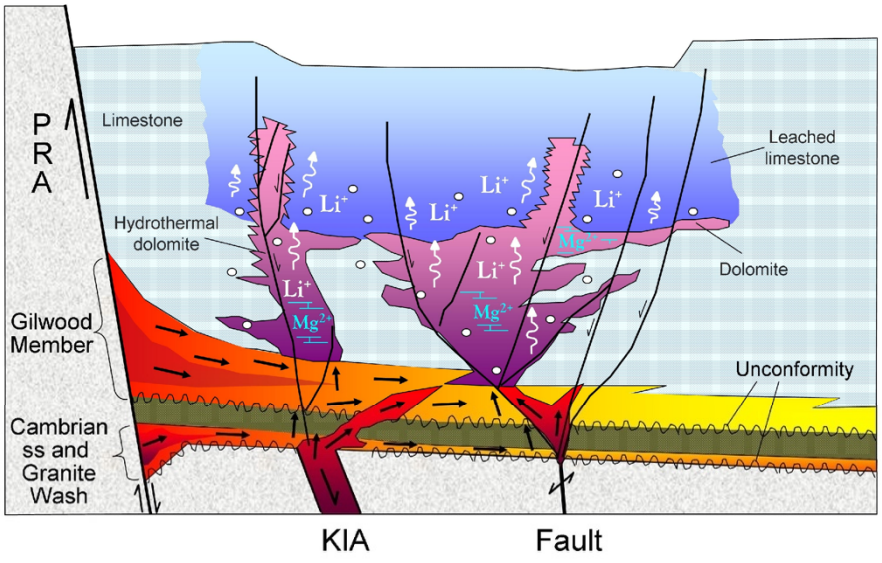

(b)

Figure 1: Lithium concentrations in lithium bearing formation waters in Alberta (a) and an illustration of mobilization of fluids along immature siliciclastics deposited above the basement and entry into the Fox Creek aquifers via fault and fracture systems (b). (Figure adapted from Eccles and Berhane[11]).

1.4. Hydraulic Fracturing Flowback and Produced Water

Hydraulic fracturing flowback and produced water (FPW) is a waste by-product of the natural gas industry.[15-17] During the fracturing process, fracturing fluid, which consists of water, sand and fracturing additives, is injected into a target geologic formation in order to fracture the rock and extract hydrocarbons.[16,17] As a result of this process, the fracturing fluid interacts with the natural formation, interstitial water, and hydrocarbons, and a fraction of the resulting fluid returns to the surface as FPW.[15,17] The formation water in hydraulic fracturing plays is often saline, typically having in excess of 100,000 ppm of total dissolved solids (TDS)[17], and bears lithium, in some cases in excess of 100 ppm.[13] In the Fox Creek region of Alberta, lithium concentrations in the formation water typically exceed 75 ppm, the highest lithium concentration reported in this region being 140 ppm.[11] Consequently, hydraulic fracturing supplies a mechanism of delivering lithium-bearing formation water to the surface, and therefore provides an opportunity for lithium recovery.

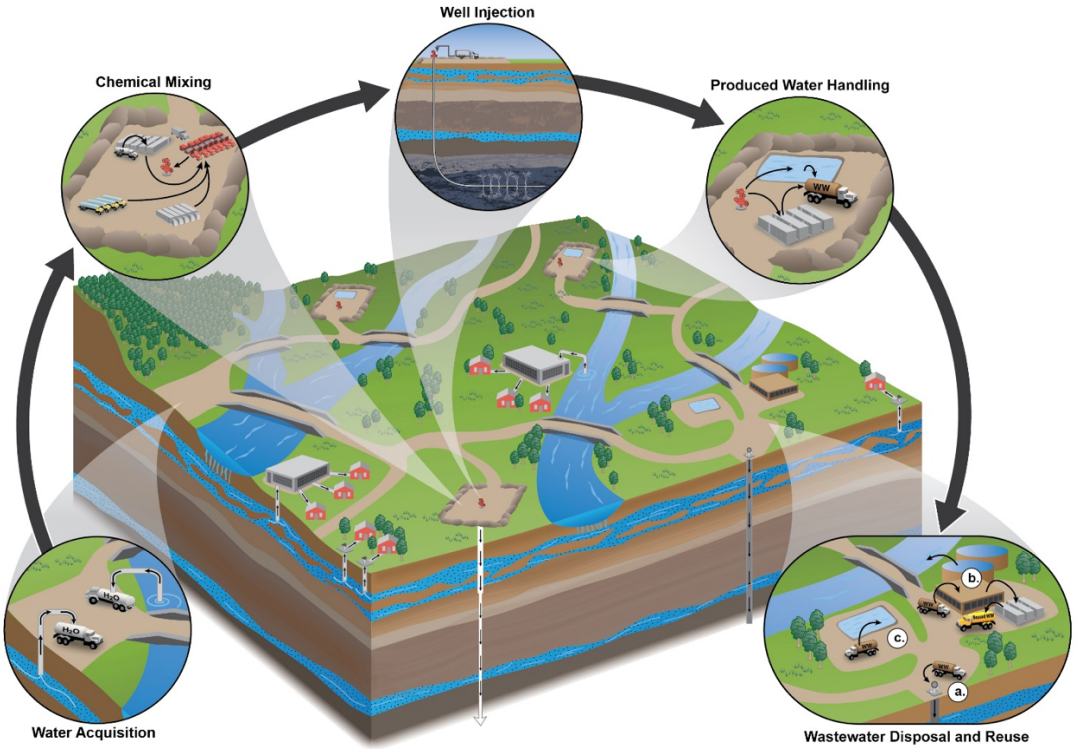

Figure 2: Schematic of water cycle in hydraulic fracturing wells, and production of FPW (Figure adapted from U.S. EPA[18]).

1.5. Lithium Recovery Methods from Brine

Common methods for lithium recovery from brine include solvent extraction, electrochemistry, solar evaporation and ion exchange.[19] The applications, benefits and drawbacks of each of these methods are described below.

1.5.1. Solar Evaporation

The solar evaporation method is the primary method of commercial scale lithium recovery from brines.[1,19,20] It is currently being used for lithium recovery from high lithium bearing Salars in South America.[1,19,20] In this method, brines with high lithium concentrations

(often > 1000 ppm) are pumped into large evaporation pools and the water is evaporated down using dry wind and high levels of solar radiation until lithium concentrations exceed 6000 ppm.[1,19,20] Sodium and potassium are typically far more abundant than lithium in these brines; for this reason, successive evaporation pools are used in order to precipitate and remove Na and K as the brine concentrates.[19,20] When the lithium concentration reaches 6000 ppm,[19] the brine is pumped to a recovery plant where borates and magnesium ions are removed using solvent extraction and precipitation with lime, respectively.[19] The brine is then treated with sodium carbonate in order to precipitate the desired product, lithium carbonate.[19] Initial lithium carbonate purities are typically 50-80%;[20] redissolution and reprecipitation cycling is required in order to reach battery grades of 99.6%.[19,20]

This method has several drawbacks; the large volume of aquifer water required to be pumped to the surface and the large land area required for the evaporation ponds may lead to negative environmental impacts, it takes considerable time to produce the final product (1-2 years), and the process often has relatively low lithium recovery efficiency (50-70%).[1,19,20] Furthermore, high magnesium concentrations in the brine increase the cost and decrease the recovery efficiency of the process, and the process is not suitable when magnesium to lithium ratios exceed 20.[20]

Because of the fact that this method requires a warm, dry climate, an excess of solar radiation, high lithium concentrations and low concentrations of divalent cations,[1,19,20] the solar evaporation method is not suitable for lithium recovery from FPW in Canada.

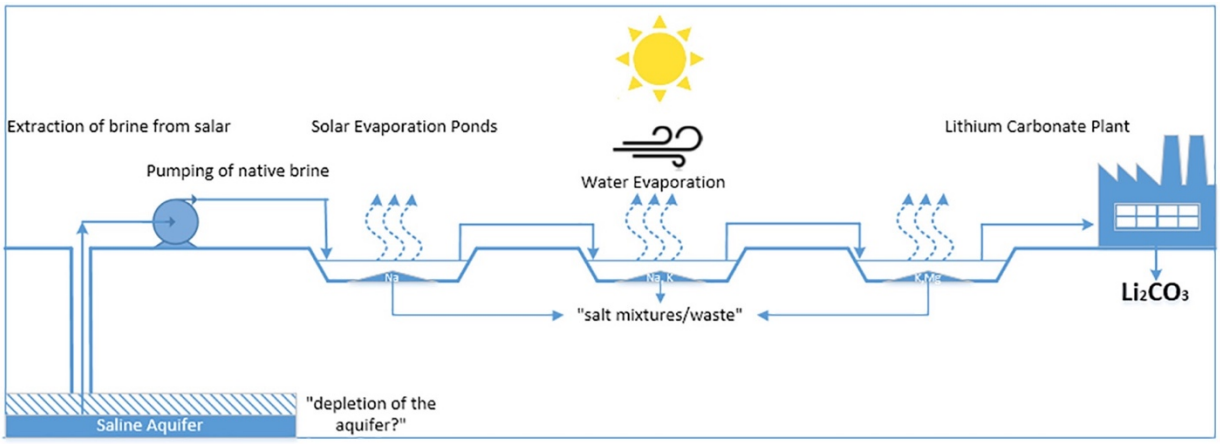

Figure 3: Schematic of Solar Evaporation method of lithium recovery. Adapted from Flexer *et al.*[19]

1.5.2. Solvent Extraction

Solvent extraction is a lithium recovery method which utilizes an organic solvent that contains a coordinating oxygen atom that extracts cations from aqueous solutions using an ion pair extraction mechanism.[14] In this method, a non aqueous phase solvent with a high affinity for lithium is added to a lithium bearing brine and the two solutions are mixed.[14,21] Lithium ions (along with other cations) from the aqueous solution bind to the coordinating oxygen on the organic solvent, and thus are recovered from solution.[14] The non aqueous lithium bearing organic solvent is then physically separated from the aqueous phase, and the lithium ions can be stripped from it using a countercurrent flow of water.[22] The isolated lithium can then be recovered as a salt by evaporation.[22]

Major disadvantages of this method include the fact that a massive amount of organic solvent would be required for lithium recovery in a commercial process, which would have significant environmental implications.[14] Potentially the most significant issue with solvent extraction as it relates to lithium recovery from brines is its low cation extraction efficiency in

highly saline solutions such as FPW; because of this, significant dilutions (up to 50 times dilution in water) are required prior to lithium recovery.[14] Even after dilution, the highest lithium recovery from a synthetic lithium bearing FPW achieved by Jang *et al.*[14] was only 41.2%. In addition to issues around low recovery efficiencies, selecting an appropriate solvent can be a challenge; most solvents which are able to separate lithium from divalent cations also have a high affinity for sodium, which is typically far more abundant than lithium in brines.[14] One of the more promising solvents, D2EHPA, has the highest reported affinity for lithium as compared to other monovalent cations;[14,21] however, this solvent has a stronger affinity for divalent cations than it does for lithium.[14,21] This means that magnesium and calcium would have to be removed prior to lithium recovery using this technology.[21] For these reasons, the solvent extraction method is not considered to be suitable for commercial scale lithium recovery from FPW at present.

1.5.3. Electrochemistry

Electrochemical lithium extraction from lithium bearing brine works in a similar fashion to the recharging of a lithium ion battery. An electric current passes from an inert electrode to a lithium selective electrode, such as λ-MnO_2, causing cations in solution to move toward the cathode.[23,24] λ-MnO_2 is selective to lithium ions, causing lithium to be sorbed by the cathode material.[23,24] After lithium extraction, the treated brine is removed from the reactor, and lithium is desorbed from the λ-MnO_2 electrode by reversing the direction of the electric current, creating a final product of isolated lithium ions in solution.[24]

The major drawbacks to this method as it pertains to lithium recovery from FPW are that it requires energy input in order to isolate the lithium,[24] and that there can be scaling issues due

to divalent cations coating the λ-MnO_2 electrode, which blocks lithium sorption sites and significantly hinders lithium recovery.[23] Additionally, this method has low efficiency when used in brines which have high concentrations of sodium and potassium.[25] This method would therefore not be considered to be suitable for low lithium bearing brines with high concentrations of divalent cations and other impurities such as FPW.[23,25]

1.5.4. Selective Adsorption

Selective ion exchange adsorbents used for lithium recovery include both titanium-based and manganese-based materials.[25] Both of these types of selective adsorbents are considered "ionic sieves" which are selective to the small ionic radii of lithium ions.[26] These materials undergo a pH dependent ion exchange reaction between protons and lithium ions,[26] as illustrated in Figure 4. The sorbent is dispersed in a lithium bearing brine where it selectively sorbs lithium ions into its structure. The sorbent is then removed from solution and the lithium ions are desorbed in acid to create a final lithium rich acidic product. Because of their high selectivity toward lithium, high lithium extraction efficiency, and fast recovery times, ion exchange adsorbents are the most promising technology for lithium recovery from low lithium bearing brines with high concentrations of impurities.[25,27]

Spinel manganese-based ion exchange sorbents represent one of the most promising lithium recovery technologies from low lithium bearing brines due to their high selectivity toward lithium and their high lithium uptake.[27] These materials have displayed the highest lithium uptake in literature of any inorganic sorbent, with experimental lithium uptake capacities in excess of 40 mg/g reported in literature.[28] The primary challenge in commercialization of these manganese-based ion exchange materials has been sorbent loss during lithium desorption

in acid.[29] Identifying major parameters which affect sorbent loss and investigating potential mitigation strategies for application in FPW is therefore critical to the economic use of these sorbents for lithium recovery.

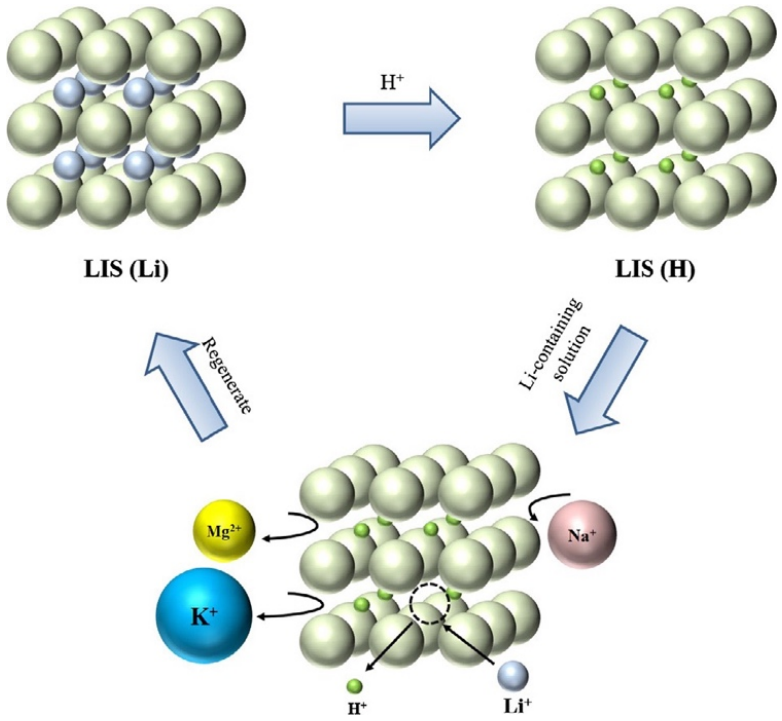

Figure 4: Lithium ion sieve extracting lithium from brine via its pH dependent ion exchange property. Adapted from Xu *et al*.[26]

1.6. Spinel Lithium Manganese Oxide

Spinel lithium manganese oxides have the general chemical formula (Li)[$Li_xMn_{2-x}O_4$], $0 \leq x \leq 0.33$, where ( ) represents the 8a tetrahedral sites and [ ] represents the 16d octahedral sites of the cubic close packed oxygen framework.[30,31] The manganese in these compounds can exist in both its trivalent and tetravalent state, and the ratio of Mn (III) to Mn (IV) determines the compound's chemical formula.[27,30-34] This ratio depends on the synthesis conditions of the

material.[30] Treatment of spinel lithium manganese oxide in acid desorbs the lithium ions from the material, creating an ionic sieve which is able to selectively extract lithium ions from aqueous media.[26,36,37] Their high selectivity toward lithium makes these materials very attractive to both the lithium ion battery and lithium extraction industries.[38] These materials are selective toward exclusively lithium due to the small ionic radii of lithium ions relative to other cations.[26,36,37] Although magnesium ions have a similar ionic radius to lithium ions (Li^+ has a 0.074 nm radius compared to an ionic radius of 0.072 nm for Mg^{2+}),[26] magnesium ion insertion is avoided in lithium ion sieves due to the high dehydration energy of magnesium ions (over 4 times higher than that of a lithium ion).[26]

Spinel lithium manganese oxides sorb lithium from solution via two reversible mechanisms: an ion exchange mechanism and a redox mechanism.[30] At an ion exchange site, a lithium ion is replaced with a proton under acidic conditions, and a proton will be replaced by a lithium ion under alkaline conditions.[26,36,37] At a redox site, the insertion of lithium under alkaline conditions results in the reduction of tetravalent manganese to trivalent manganese in the spinel structure.[27,30] When the lithium inserted redox site is exposed to acid during lithium desorption, the release of lithium ions is accompanied by the disproportionation reaction $2\ Mn^{3+} \rightarrow Mn^{4+} + Mn^{2+}$.[27,30] This results in the reductive dissolution of structural Mn (III) to aqueous Mn (II), and a consequential net loss of sorbent.[27,30]

The proportion of ion exchange sites to redox sites in a specific lithium manganese oxide is dependent on the average oxidation state of the manganese. Sorbents with higher proportions of trivalent manganese, such as $LiMn_2O_4$, will have a higher proportion of redox sites, whereas a sorbent with exclusively tetravalent manganese, such as $Li_{1.33}Mn_{1.67}O_4$, will have almost exclusively ion exchange sites.[27,30-34] In order to avoid the reductive dissolution of manganese

with each sorption-desorption cycle, the optimum spinel lithium manganese oxide structure for lithium extraction is a pure ion exchange sorbent with exclusively tetravalent manganese.[36]

Examples of such a material are both $Li_{1.33}Mn_{1.67}O_4$, and lithium rich spinel manganese oxide, which has the formula $Li_{1.6}Mn_{1.6}O_4$. Lithium rich spinel lithium manganese oxide deviates from the general $(Li)[Li_xMn_{2-x}O_4]$, $0 \leq x \leq 0.33$ formula for spinel lithium manganese oxides, and is thought to have the structure of a hexagonal lattice with cation deficiency.[31,38] This material has displayed the highest experimental lithium sorption capacity of any ion exchange sorbent.[38]

Due to their lithium selective nature, spinel lithium manganese oxides can be used to extract aqueous phase lithium ions from brines with high concentrations of other cations.[36] Lithium insertion into the spinel structure is highly dependent on factors such as pH and lithium concentration, as well as the dosage of sorbent into the fluid.[39,40] Generally, low pH drives the ion exchange in the direction of lithium desorption, and so lithium extraction is significantly impeded when the fluid pH drops below 6.[39] As Figure 5 illustrates, lithium uptake by the sorbent increases with increasing alkalinity until a fluid pH of approximately 8, where lithium insertion begins to plateau.[39] Figure 5 also illustrates that although lithium uptake drops dramatically at very low lithium concentrations, lithium uptake is generally not highly dependent on lithium concentration; this makes manganese-based lithium adsorbents a good choice for application in low lithium bearing brines such as FPW.

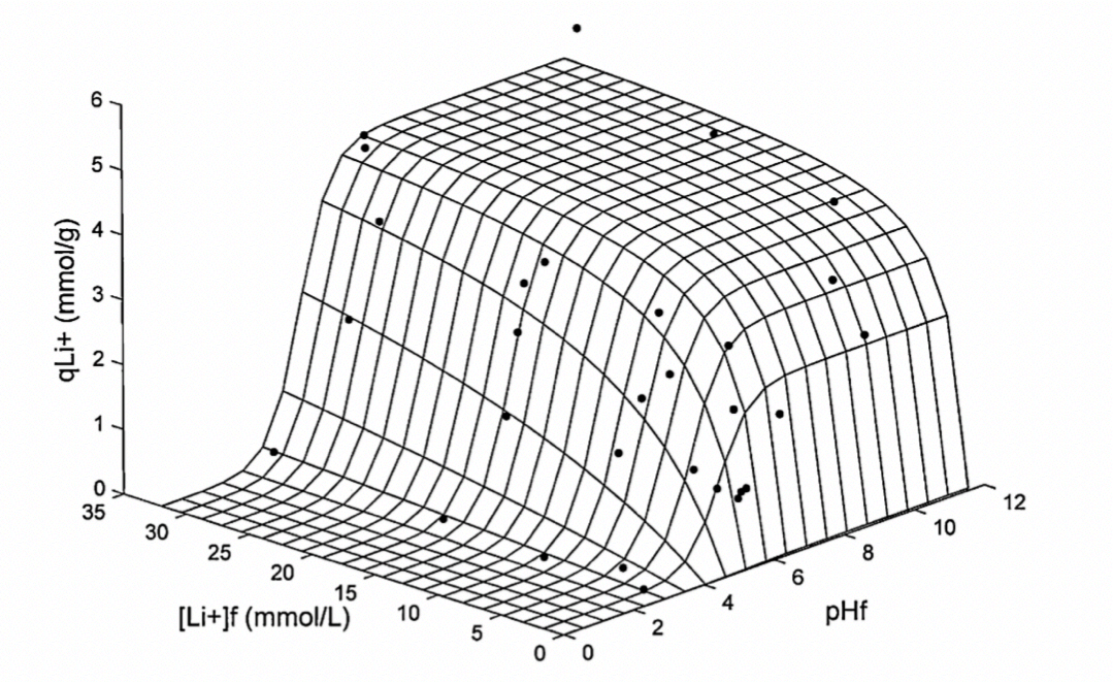

Figure 5: Lithium uptake (qLi^+) vs. lithium concentration ($[Li^+]f$) and pH (pHf) of initial LiCl solution. (Figure adapted from Tian *et al.*[39])

The theoretical maximum uptake of lithium into protonated lithium rich manganese oxide ($H_{1.6}Mn_{1.6}O_4$) would be 73 milligrams of lithium per gram of sorbent, if all protons in the sorbent were replaced with lithium ions.[36] Such an uptake has not been achieved experimentally, however, as lithium reinsertion occurs only at the tetrahedral sites, and not at the octahedral sites, of the protonated sorbent.[38] The highest lithium uptake values which are able to be consistently achieved in literature are between 35 to 40 mg g^{-1}.[31,36,38,39]

1.7. Previous Work

There have been numerous studies which explore the synthesis and characterization of manganese-based lithium adsorbents.[27,30-35,38] There have also been studies conducted which employ these materials for the recovery of lithium from seawater[29,41] and from brine lakes.[42] Jang *et al.*[13] employed a titanium-based ion exchange sorbent, and Jang *et al.*[14] employed a solvent extraction method, to recover lithium from laboratory synthesized FPWs. The titanium-based sorbent employed by Jang *et al.*[13] was effective at selectively adsorbing lithium, however the process was slow (24 hour sorption time), and lithium recovery was < 60%. The solvent extraction method used by Jang *et al.*[14] was ineffective for the purpose of lithium recovery from high TDS brine, with a low lithium recovery of 41.2% even after the brine was diluted 50:1 in water.

There are not extant studies which utilize a manganese-based sorbent for lithium recovery from FPW. Furthermore, it is not understood how the complex organic profile, which is present in the FPW due to both fracturing additives and organics indigenous to the fractured hydrocarbon-bearing formation,[12] affects this lithium recovery technology.

1.8. Research Purpose and Objectives

The objectives of this research are as follows:

1. To prepare two manganese-based lithium adsorbents using different synthesis conditions and perform a comprehensive materials characterization on each to determine the effect of synthesis conditions on the sorbent chemical and physical structure.

2. To perform a series of lithium recovery experiments from field collected FPW, varying different parameters in order to determine a set of optimized conditions for lithium extraction. Parameters which will be tested include sorption pH, sorption temperature, sorption time, sorbent dosage, desorption time, and desorption acid concentration. Performance will be evaluated based on maximizing lithium uptake and recovery and minimizing sorbent loss, along with maximizing the purity of the final acidic product.

3. To utilize both manganese-based sorbents to recover lithium from field collected FPW samples at pre-determined optimized sorption conditions in order to determine the effect of synthesis conditions and sorbent structure on the lithium recovery process.

4. To compare the performance of each manganese-based sorbent on lithium recovery from both field collected FPW and from a synthetic lithium-bearing brine in order to determine the effect which the complex organic profile in the FPW has on manganese-based sorbents during lithium recovery using this technology.

My hypotheses related to this project are as follows:

1. After optimization, the manganese-based sorbents synthesized for this work will show promising results when used in FPW, exhibiting high lithium uptake and high selectivity for lithium.

2. Organic molecules in the FPW will inhibit the lithium recovery process, and lithium uptake will be higher when using the synthetic brine compared to when using the field collected FPW.

2. Materials and Methods

2.1. Reagents

Lithium hydroxide (98%), manganese chloride tetrahydrate ($MnCl_2 \bullet 4H_2O$, > 99%), hydrogen peroxide (H_2O_2, 30% in water), sulfuric acid (H_2SO_4, 98%), sodium hydroxide (NaOH, > 99%), ammonium oxalate monohydrate ($(NH_4)_2C_2O_4 \bullet H_2O$, > 99%), potassium permanganate ($KMnO_4$, > 99%), hydrochloric acid (HCl, 37% in water), sodium chloride (NaCl, > 99%), lithium chloride (LiCl, > 99%), microcrystalline cellulose, Triton X-100 (70% in water), Boric acid (H_3BO_3, > 99%), magnesium chloride hexahydrate ($MgCl_2 \bullet 6H_2O$, > 99%), potassium chloride (KCl, > 99%), sodium bicarbonate ($NaHCO_3$, > 99%), strontium chloride hexahydrate ($SrCl_2 \bullet 6H_2O$, > 99%), calcium chloride dihydrate ($CaCl_2 \bullet 2H_2O$, > 99%), and manganese dioxide (MnO_2, 98%) were purchased from Fisher Scientific, Canada. Lithium manganese dioxide ($LiMnO_2$, > 99%) and lithium manganese (III, IV) oxide ($LiMn_2O_4$, > 99%) were purchased from Sigma Aldrich, Canada. All solutions were prepared using deionized water with a resistivity of 18.2 MΩ cm at 25°C.

2.2. Flowback and Produced Water

The FPW used in this study was collected in the field from a hydraulically fractured well in the Duvernay formation near the town of Fox Creek, Alberta, Canada in December 2016. The FPW was collected 15 days after fracturing. A synthetic brine was prepared to mimic the inorganic properties of the FPW. Major properties of the fluids are listed in Table 1.

Table 1: Physical properties and major ion concentrations of FPW and synthetic brine. Sodium bicarbonate was added to the synthetic brine in order to replicate the experimental buffering ability of the FPW.

Parameter	Field Collected FPW	Synthetic Brine
TDS	184 000 ppm	180 000 ppm
NPOC	180 ppm	4 ppm
Density	1.124 g mL^{-1}	1.123 g mL^{-1}
Li	43 ppm	43 ppm
B	69 ppm	75 ppm
Na	55 000 ppm	57 000 ppm
Mg	820 ppm	860 ppm
K	1 600 ppm	1 600 ppm
Ca	9 700 ppm	10 000 ppm
Sr	930 ppm	880 ppm
TIC (as CO_3^{2-})	BDL	24 ppm

For experiments on filtered fluid samples, FPW was centrifuged at 4000 g for 5 min and the oil layer was removed using a pipette. The fluid was then filtered through a 0.20 μm nylon syringe filter before ultra or nanofiltration. For ultrafiltration, the filtered FPW was passed through a Millipore Pellicon XL Cassette Biomax 10 kDa ultrafiltration membrane using a peristaltic pump, and for nanofiltration the FPW was passed through a 100-250 Da Synder Filtration NFS nanofiltration membrane using dead stop filtration at 5 bar. Major properties of filtered fluids are listed in Table 2.

Table 2: Major ion concentrations and NPOC of Ultrafiltered (UF) and Nanofiltered (NF) FPW.

Parameter	UF FPW	NF FPW
NPOC	116 ppm	85 ppm
Li	42 ppm	45 ppm
B	68 ppm	69 ppm
Na	56 000 ppm	53 000 ppm
Mg	810 ppm	500 ppm
K	1 700 ppm	1 600 ppm
Ca	10 000 ppm	8 900 ppm
Sr	900 ppm	740 ppm

2.3. Sorbent Preparation

Manganese-based sorbents were prepared using a co-precipitation method similar to that used by Tian *et al*.[39] 3.0 M LiOH was added in Li:Mn molar ratios of 2:1 and 3:1 to 0.375 M $MnCl_2$ solution at 20°C to produce a slurry of $Mn(OH)_2$. The resulting final sorbents were designated as LMO-2 and LMO-3, respectively. 30% H_2O_2 was added dropwise to each solution in a H_2O_2:Mn molar ratio of 10:1 to oxidize the Mn (II) and produce the manganese oxide precursor. Each solution was stirred for 2 h, transferred to a ceramic drying tray and dried in a forced air convection oven at 90°C for 16 h. The resulting precursors were ground to a fine powder using a mortar and pestle and calcined in a furnace in air at 450°C for 4 h. Each sorbent was then washed twice in deionized water, and the resulting products were designated lithium manganese oxides LMO-2 and LMO-3. Portions of each of these materials were stirred in 0.50 M H_2SO_4 at 20°C for 1 h at a sorbent dosage of 10.0 g L^{-1}. The resulting protonated ionic sieves were washed twice in deionized water and designated as HMO-2 and HMO-3 for synthesis Li:Mn ratios of 2:1 and 3:1, respectively.

2.4. Sorption and Desorption Experiments

Optimization of lithium recovery conditions was performed as part of this study and can be referenced in section 3.2.1. FPW was centrifuged at 4000 g for 5 min and the oil layer was removed using a pipette. The FPW was pipetted into a glass vial, and its pH was adjusted using 1.0 M NaOH. pH was measured using a Mettler Toledo FiveEasy Plus pH meter. The FPW was heated to 70°C, and protonated sorbent was added at a dosage of 2.0 g L^{-1} for a sorption time of 30 min with constant mixing. After sorption, the mixture was centrifuged at 4000 g for 5 min.

The treated FPW was removed and the Li loaded sorbent was washed twice with deionized water. The Li loaded sorbent was then added to 0.5 M H_2SO_4 at a dosage of 6.0 g L^{-1} and was stirred at 20°C for 5 min. After desorption, the mixture was centrifuged at 4000 g for 5 min. The acid was removed, the re-protonated sorbent was washed twice with deionized water, and the sorbent was dried in open air at 20°C.

FPW samples were taken after pH adjustment and after treatment and were analyzed for major elements using an Agilent 8800 Triple Quad Inductively Coupled Plasma – Mass Spectrometer (ICP-MS/MS). Elements measured in the FPW were Li, B, Na, Mg, K, Ca and Sr. Li uptake was determined using a mass balance between the pH adjusted and treated FPW. A sample of the desorption acid was analyzed using ICP-MS/MS for the same elements measured in the FPW samples to determine the lithium concentrate purity, as well as for Mn to calculate sorbent loss in the acid.

2.5. Chemical Analyses

2.5.1. Manganese Average Oxidation State Determination

Manganese average oxidation state (Z_{Mn}) was determined using a method similar to that outlined by Freeman and Chapman.[43] 180 mg of sorbent was digested in 25 mL of 0.10 M $(NH_4)_2C_2O_4$ + 12.5 mL of 4.0 M H_2SO_4 at 80°C until complete dissolution was reached. The digestions were then back-titrated using 0.010 M $KMnO_4$ to a faint pink endpoint in order to determine the moles of oxalate which reacted, and therefore the moles of electrons which were transferred during the digestion step.

Mass percentages of Mn and Li in each sorbent were determined by digesting 40 mg of sorbent in 20 mL of 6.0 M HCl + 1.0 mL of 30% H_2O_2 at 80°C for 1 h. Samples were then analyzed for Mn and Li concentrations using ICP-MS/MS; subsequently, the total moles of Mn in the sorbent used in the oxalate digestion was determined. Z_{Mn} was then calculated using the total moles of Mn in conjunction with the total moles of transferred electrons between oxalate and Mn determined by the titration. The Li:Mn molar ratio determined using ICP-MS/MS, in combination with Z_{Mn}, was then used to calculate a chemical formula for each sorbent in the form of $Li_xMn_yO_4$.[30]

2.5.2. Li Selectivity Titrations

Selectivity titrations were performed using a method similar to that outlined by Ooi *et al*.[32] 50 mg portions of protonated sorbent were added to 5.0 mL of 0.10 M solutions of MOH + MCl (M = Li or Na) in varying ratios of hydroxide to chloride. Blank titrations of NaOH + NaCl in the absence of sorbent were also prepared. The mixtures were stirred on a shaker table at 375 rpm at 20°C for 6 h, and the pH of the supernatant of each solution was measured after sorption. Samples of the Li solutions were taken before and after sorption and analyzed using ICP-MS/MS to determine maximum uptake.

2.6. Physical Analyses

Fourier-transform infrared spectroscopy (FTIR), thermogravimetric analysis (TGA) and X-ray diffraction (XRD) were all performed on 10 mg samples of dry sorbent. FTIR was performed using a Bruker Alpha FTIR Spectrometer, and absorbance values were collected in

the wavenumber range of 750 – 4000 cm^{-1}. TGA was performed using a TA Instruments TGA Q50 using nitrogen gas, increasing the temperature from 20°C – 1000°C at a rate of 10°C min^{-1}. XRD patterns were obtained using a Rigaku Ultima IV with a cobalt tube radiation source at 38 kV and 38 mA. Scans were performed using a range of 5°– 90° and a step size of 0.0200°. XRD patterns were interpreted and converted to a copper source using JADE 9.6 software.

Mn K-edge X-ray absorption spectroscopy (XAS) measurements were performed at beamline B18 at the Diamond Light Source, U.K. Samples were prepared by diluting 5 mg of sorbent in 150 mg of microcrystalline cellulose and mixing using a mortar and pestle. The mixture was then pressed into a 13 mm diameter pellet using a hydraulic press. Incident X-ray wavelengths were selected using a fixed exit double-crystal monochromator (with Si(111) and Si(311) crystals).[44,45] XAS spectra were collected in transmission mode using two gas-filled ionisation chambers.[44,45] Mn metal foil was placed in front of a third ionisation chamber in order to correct for instrument drift.[45] For each sample, scans were performed in triplicate and the data were averaged and normalised using the program ATHENA[46] to produce X-ray absorption near edge structure (XANES) and extended X-ray absorption fine structure (EXAFS) spectra. k^3 weighted EXAFS spectra were modelled using ARTEMIS software, which uses structural models produced from published crystal structures,[46] to determine interatomic Mn-O and Mn-Mn distances within each sample. Z_{Mn} from XANES spectra were determined using linear combination modelling in ATHENA; $LiMnO_2$, $LiMn_2O_4$ and MnO_2 were used as reference materials for Z_{Mn} of 3.0, 3.5 and 4.0 respectively.

A Kratos Ultra DLD X-ray Photoelectron Spectrometer (XPS) was used to acquire the near surface (<10 nm) elemental composition and manganese oxidation states. A monochromatic Al source was used at 150 W power to obtain survey scans and Mn 2p, Mn 3p, and Mn 3s high

resolution spectra from the near surface region. The pass energy for narrow scans was 20 eV. Charge neutralization was used during acquisition. 99.9% pure Au reference powder was used to calibrate the spectra for Au $4f_{7/2}$ to 84.0 eV. Three areas per samples were analyzed; average and standard deviations are reported. Shirley background was used to process the spectra. Quantification utilized sensitivity factors that were provided by the manufacturer. A 70% Gaussian / 30% Lorentzian (GL (30)) line shape was used for the curve fittings. Constraints used in curve fitting of Mn 2p, Mn 3p, Mn 3s spectra were established in a previous study.[24] Multiplet splitting of Mn 3s high resolution spectra was used to determine the oxidation state of Mn as described in a previous study.[47] Additionally, the oxidation state of Mn was confirmed by observing the shape and position of Mn 3p high resolution spectra.

Transmission electron microscope (TEM) images were acquired using a Philips/FEI (Morgagni) TEM along with a Gatan digital camera. Sorbent samples were dispersed in a 0.10 mg mL^{-1} suspension and a drop of the suspension was placed onto a TEM grid for analysis. Nitrogen adsorption/desorption isotherms at 77 K were obtained using a Quantachrome Autosorb-iQ-MP/XR and specific surface area was calculated using the Brunauer-Emmett-Teller (BET) method.[48] Prior to analysis, each 200 mg sorbent sample was outgassed at 200°C for 6 h. Zeta potential was measured using a Malvern Zetasizer. Samples measured were 0.10 mg mL^{-1} suspensions of sorbent in deionized water at varying pH values. pH was adjusted using HCl or NaOH.

2.7. Fluid Analyses

Fluid samples for both non-purgeable organic carbon (NPOC) and total inorganic carbon (TIC) analyses were diluted 50:1 (v/v) in deionized water prior to analysis. A Shimadzu TOC-L

CPH Model Total Organic Carbon Analyzer with an ASI-L TOC autosampler was used for both analyses. For NPOC measurement, samples were acidified using 1 M HCl before being sparged in order to strip the sample of purgeable organic and inorganic carbon. The sample was subsequently injected into a combustion tube containing platinum catalyst beads at 720°C in order to evolve the remaining carbon in the sample to CO_2, which was then measured using a non-dispersive infrared (NDIR) detector. For TIC measurement, the sample was injected into a bubble chamber, and phosphoric acid (25%) was added to react with the inorganic carbon, forming CO_2 gas. The sample was bubbled with air, and the evolved CO_2 was measured using an NDIR detector.

3. Results and Discussion

3.1. Characterization of Initial Sorbents

3.1.1. Structural Analysis

As stated previously, spinel lithium manganese oxides sorb lithium via two proposed reversible sorption mechanisms: a redox mechanism and an ion exchange mechanism, as can be seen in Equations 1 and 2 respectively (represents an empty space in the crystal).[27,30]

$$4(Li)[Mn^{3+}Mn^{4+}]O_4 + 8H^+ \rightarrow 3(\ )[Mn^{4+}{}_2]O_4 + 4Li^+ + 2Mn^{2+} + 4H_2O \quad (1a)$$

$$(\ )[Mn^{4+}{}_2]O_4 + n\text{LiOH} \rightarrow (Li_{n}\ {}_{1-n})[Mn^{3+}{}_n Mn^{4+}{}_{2-n}]O_4 + \frac{n}{2}H_2O + \frac{n}{4}O_2 \quad (1b)$$

$$Li_xMn_yO_4 + xH^+ \leftrightarrow H_xMn_yO_4 + xLi^+ \quad (2)$$

These materials are selective toward lithium (under alkaline conditions) and protons (under acidic conditions) due to the small ionic radii of lithium ions and of protons.[26,36,37] Manganese in these sorbents can exist in both trivalent and tetravalent states; materials with higher proportions of trivalent manganese have a higher proportion of redox sites, while sorbents with exclusively tetravalent manganese contain exclusively ion exchange sites.[27,30-34] At a redox site, lithium desorption in acid is associated with reductive dissolution of trivalent to divalent manganese (Equation 1a), resulting in a net loss of sorbent with each sorption/desorption cycle.[27,30] For this reason, the optimum, highest stability manganese-based sorbent would contain exclusively tetravalent manganese.[36]

Z_{Mn} of sorbent LMO-2 and its protonated counterpart HMO-2 were determined to be 3.47 and 3.64, respectively, indicating a significant proportion of Mn (III) in their structures. The resulting chemical formula calculated for LMO-2 is $Li_{0.91}Mn_{2.04}O_4$. The prevalence of Mn (III) in the structure indicates the presence of redox sites in this sorbent.[30-35] LMO-3 and HMO-3 had Z_{Mn} of 3.87 and 3.99, respectively, resulting in a chemical formula of $Li_{1.47}Mn_{1.69}O_4$ for LMO-3. HMO-3's oxidation state is consistent with a sorbent with almost exclusively ion-exchange sites.[30-35] Z_{Mn} in both sorbents increased significantly after the initial protonation step due to acid dissolution of low valence manganese in the bulk material.[30,32] Dissolution of low valence manganese phases would also lead to the tighter distribution of Mn-Mn distances determined by EXAFS between the LMO and HMO versions of each sorbent (Table 3).

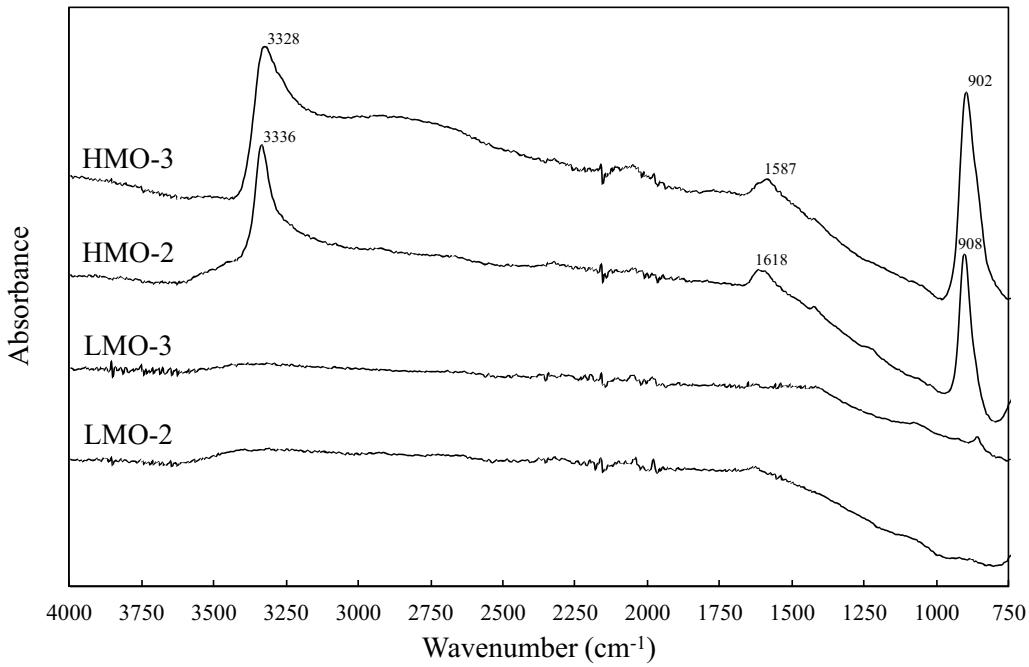

Figure 6: FTIR comparison plot of initial calcined (LMO) and protonated (HMO) sorbents.

FTIR spectroscopy (Figure 6) shows absorbance peaks at 3330 cm^{-1}, 1600 cm^{-1} and 900 cm^{-1} for both protonated sorbents which do not appear in their calcined counterparts. The absorbance peak at 3330 cm^{-1} can be attributed to stretching vibrations of hydroxyl groups within the structure, the peak at 1600 cm^{-1} is due to bending vibrations of hydroxyl groups, and the peak at 900 cm^{-1} is due to vibrations of protons.[38] These peaks demonstrate that both HMO-2 and HMO-3 experienced proton insertion into their structures during acid treatment, indicating that both sorbents contain ion exchange sites.[49]

TGA data (Figure 7) for both protonated sorbents shows mass loss between 150 – 300°C, which further indicates the presence of ion exchange sites in the sorbents.[30-33,36,38] This mass loss, centered around 220°C, has been attributed to structural water loss from condensation of hydroxyl groups, which were formed during ion exchange with lithium, within the spinel structure of the sorbent.[30,31,38] In this way, the total proton content of the protonated sorbent, and

therefore the concentration of ion exchange sites, can be determined from the mass loss between 150 – 300°C.[30] HMO-2 experienced a 1.97% mass loss in this temperature range as compared to a 6.18% loss by HMO-3, indicating that HMO-3 contains more than 3 times more ion exchange sites than HMO-2. The redox site concentration can then be calculated from the ratio of Li to Mn in the desorption acid;[30] site evaluation results are listed in Table 3. After determining proton content, chemical formulas were assigned to the protonated sorbents using the method outlined by Feng *et al*.[30]

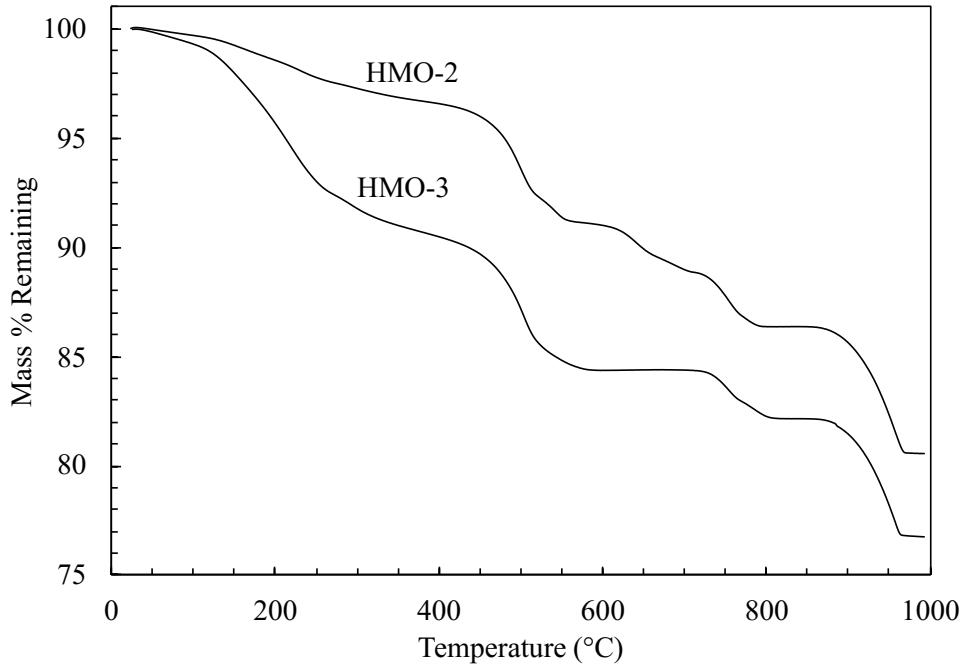

Figure 7: TGA comparison plot of initial calcined (LMO) and protonated (HMO) sorbents.

Site evaluation results for HMO-3 present a 98% proportion of ion exchange sites, which is consistent with its Z_{Mn} of 3.99.[30,32,31-34] Site evaluation results for HMO-2 shows an ion exchange site percentage of 79%, signifying that it is primarily an ion exchange sorbent as well. This is atypical given the high proportion of Mn (III) in its structure, which is associated with the

presence of redox sites.[30-35] The prevalence of Mn (III) in HMO-2 was therefore hypothesized to be dominantly in the form of a separate Mn (III) phase in the bulk material which did not participate in the lithiation/delithiation reactions. This hypothesis is supported by the Z_{Mn} increase to only 3.64 after acid treatment; in a pure redox type sorbent such as $LiMn_2O_4$, Z_{Mn} increases to 4.0 after delithiation.[30] These additional Mn (III) phases would impact the resulting chemical formulas calculated using the Feng *el al*.[30] method for LMO-2 and HMO-2; this hypothesis also helps to explain why the formula for LMO-2 falls outside of the spinel lithium manganese oxide formula range of $(Li)[Li_xMn_{2-x}]O_4$, $0 \leq x \leq 0.33$.[31]

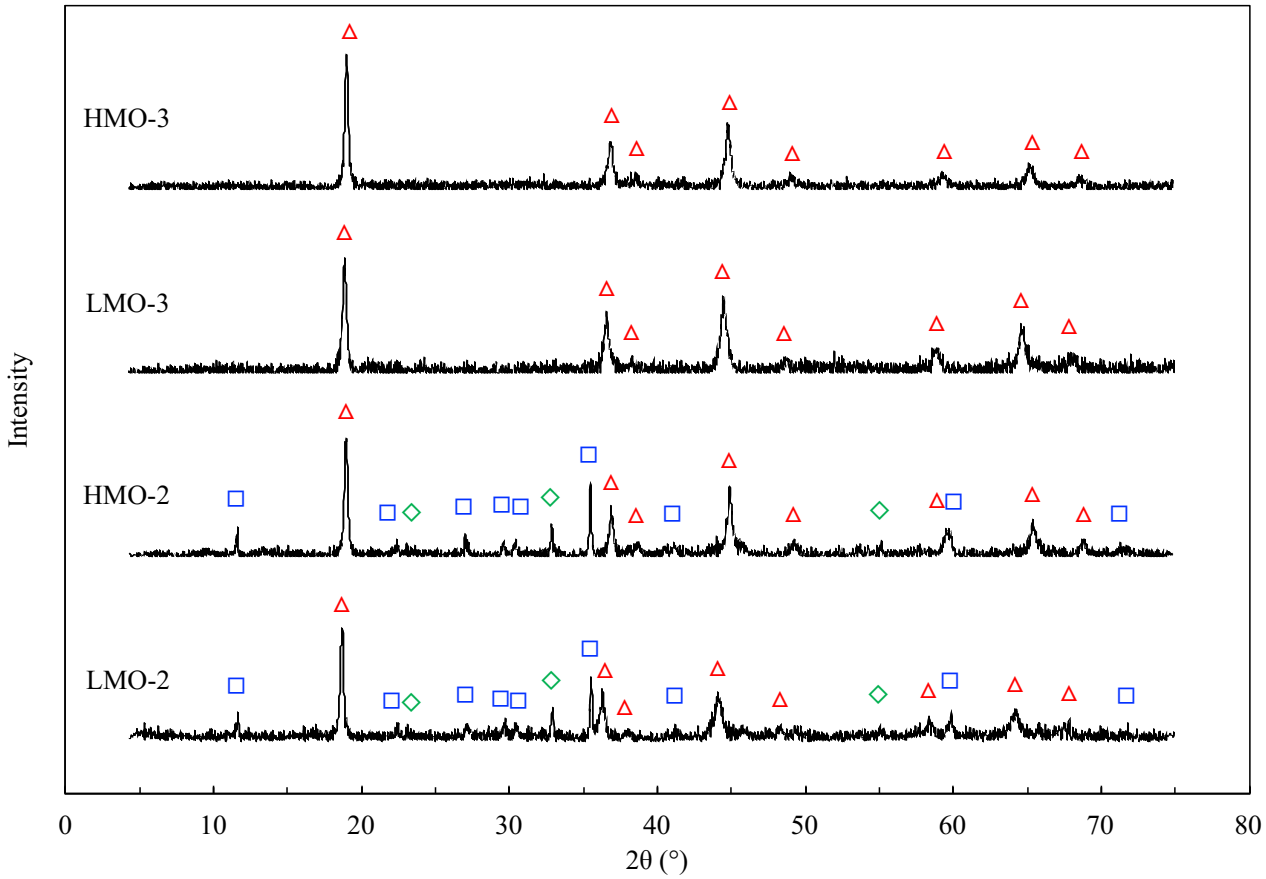

Figure 8: XRD comparison plot of initial calcined and protonated sorbents. ◇, □ and △ represent peaks which can be attributed to Mn_2O_3, $Mn_8O_{10}Cl_3$ and $Li_{1.33}Mn_{1.67}O_4$ phases, respectively.

XRD patterns (Figure 8) for LMO-3 and HMO-3 confirm its spinel structure, and display a pattern consistent with that of the ion-exchange sorbent $Li_{1.33}Mn_{1.67}O_4$. The similarity between the XRD patterns for LMO-3 and HMO-3 indicates that delithiation occurred topotactically during acid treatment, preserving the original spinel structure.[31] Three different phases were identified in the XRD patterns of LMO-2 and HMO-2: $Li_{1.33}Mn_{1.67}O_4$, Mn_2O_3 and $Mn_8O_{10}Cl_3$. The presence of one or both of these low valence manganese impurities in LMO/HMO-2 is supported by both the XPS and EXAFS analyses. EXAFS revealed a larger distribution of Mn-Mn interatomic distances in HMO-2 species compared to those in HMO-3 species (Table 3, Table B1). This could be explained by HMO-2 species being comprised of a mix of separate manganese phases. Furthermore, the LMO/HMO-2 species could not be adequately fit using EXAFS without the addition of 30% Mn_2O_3 to the $Li_{1.33}Mn_{1.67}O_4$ model (Figure 9). An addition of 30% $Mn_8O_{10}Cl_3$ to the LMO/HMO-2 EXAFS model also resulted in an adequate fit. XPS detected Mn (III) on the surface of LMO-2 (Table B3), and Cl was detected on the surface of LMO-2 during the XPS elemental mapping, consistent with XRD evidence for the presence of Mn_2O_3 and $Mn_8O_{10}Cl_3$. $Mn_8O_{10}Cl_3$ can be produced during calcination of MnO_2 + $MnCl_2$ above 300°C,[50] and so its presence is conceivable given the reagents in the co-precipitation method used. This supports my earlier hypothesis that delithiation could have occurred primarily at the ion exchange sites in the sorbent, while the Mn (III) phases were not significantly affected during acid treatment. A Z_{Mn} of 3.64 in the delithiated sorbent suggests that HMO-2 may consist of more than 30% non lithium-exchanging Mn (III) phases; it can therefore be concluded that for the co-precipitation method employed in this research, a large excess of Li (Li:Mn of 3) is required during synthesis in order to avoid production of these phases.

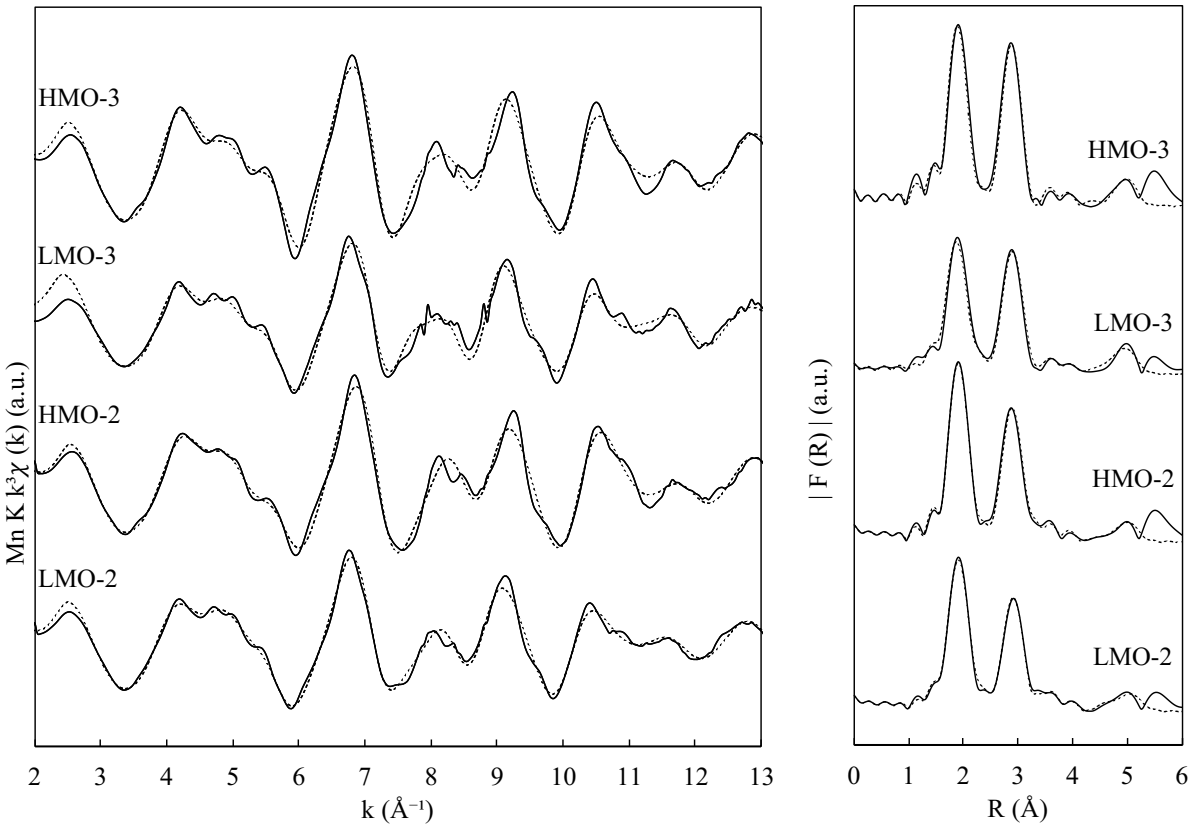

Figure 9: Mn K-edge EXAFS and Fourier transforms for initial calcined and protonated sorbents. Dashed lines represent fits for each material. LMO/HMO-3 species were fit using a pure $Li_{1.33}Mn_{1.67}O_4$ model, whereas LMO/HMO-2 species were fit using a 70% $Li_{1.33}Mn_{1.67}O_4$, 30% Mn_2O_3 model; dashed lines represent fits for each material.

EXAFS data for calcined and protonated versions of each sorbent indicate a contraction of the crystal structure of the sorbents after protonation.[51-53] This is evidenced by the decreased distance between Mn-Mn atoms between the LMO and HMO versions of each sorbent, as displayed in Table 3. These Mn-Mn distances increase again after relithiation, and subsequently decrease after lithium desorption (Table B1), suggesting that the crystal structure of the sorbent expands during lithium insertion and contracts during lithium desorption in every cycle. Similar results have been reported in previous studies[51-53] which use EXAFS analysis to study manganese-based ion exchange materials.

TEM images of both calcined and protonated sorbents are displayed in Figure 10. LMO-2 and HMO-2 appear to consist of a combination of long (>100 nm length) needle shaped particles as well as some small (<100 nm diameter) cubic shaped particles, while LMO-3 and HMO-3 are comprised of almost exclusively small, cubic shaped particles. The larger particles comprising HMO-2 result in a smaller BET surface area of 33 $m^2 g^{-1}$, compared to 74 $m^2 g^{-1}$ for HMO-3. Both sorbents' surface area more than doubles after the initial protonation step (between their LMO and HMO versions); this result was also found by Wang *et al.*[31], and can be attributed to dissolution of Mn (II) and opening of pores in the structure after first exposure to acid.[34,54] This is supported by the measured increase in pore volume in both sorbents after protonation (Table 3).

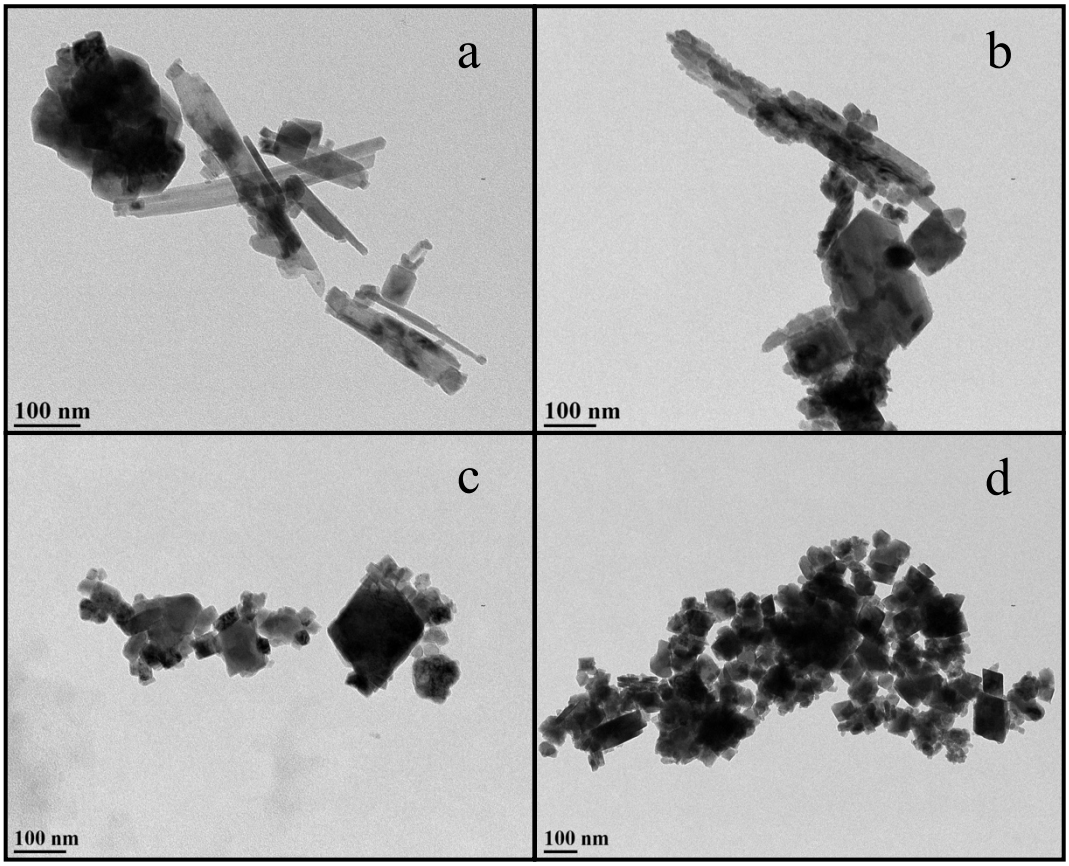

Figure 10: TEM images of LMO-2 (a), HMO-2 (b), LMO-3 (c) and HMO-3 (d).

Table 3: Summary table of physical and chemical characteristics of initial calcined and protonated sorbents.

Sorbent	Z_{Mn}	Chemical Formula (Feng *et al.*[30] method)	Ion Exchange Site Fraction	Redox Site Fraction	BET Surface Area ($m^2 g^{-1}$)	Pore Volume ($cm^3 g^{-1}$)	EXAFS Mn-Mn distances	
							R (Å)	σ (Å)
LMO-2	3.47	$Li_{0.91}Mn_{2.04}O_4$	-	-	15	0.22	2.90	0.088
HMO-2	3.64	$Li_{0.17}H_{0.42}Mn_{2.04}O_4$	79%	21%	33	0.26	2.87	0.083
LMO-3	3.87	$Li_{1.47}Mn_{1.69}O_4$	-	-	25	0.07	2.89	0.087
HMO-3	3.99	$Li_{0.12}H_{1.21}Mn_{1.67}O_4$	98%	2%	74	0.25	2.87	0.079

3.1.2. Behavior in Solution

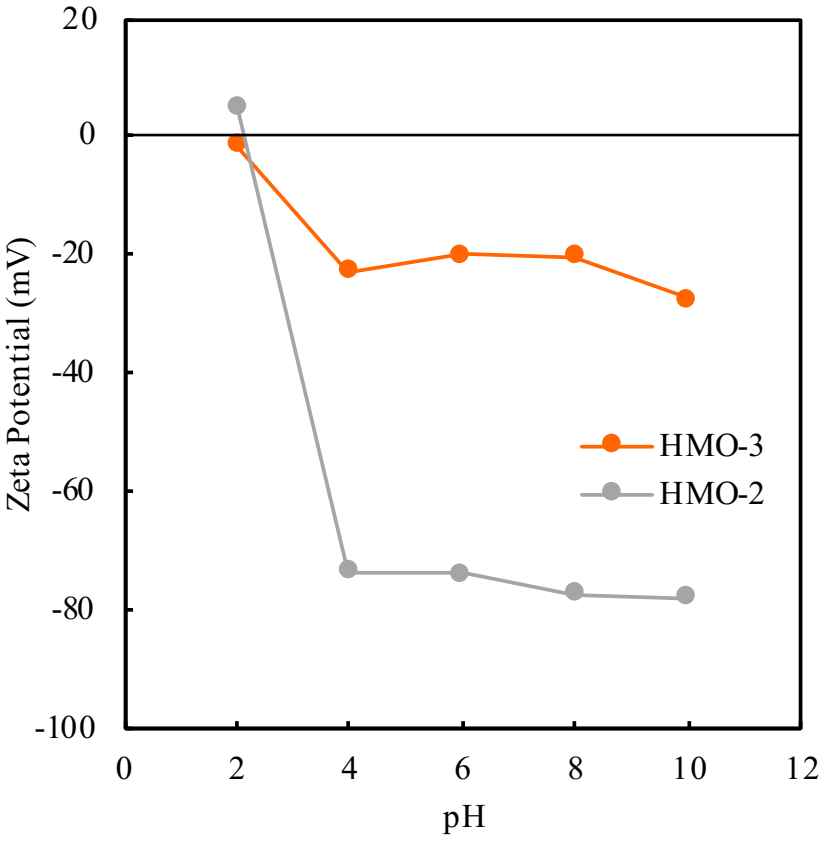

Figure 11: Zeta potential versus pH of solution of HMO-2 and HMO-3.

Both HMO-2 and HMO-3 have a point of zero charge (PZC) in solution close to pH 2 (Figure 11). This indicates that both sorbents should exhibit good dispersion at typical Li sorption conditions of pH 6 and higher.[39] HMO-2 has a significantly more negative zeta potential than HMO-3 when pH ≥ 4. HMO-3 is shown by TGA data to contain more hydroxyl groups than HMO-2; a higher concentration of hydroxyl groups would typically lead to a more negative zeta potential,[55] however, the intramolecular hydroxyl groups associated with Li-specific ion exchange sites in HMO species are not surface functional groups, and will therefore only interact with the solution if Li ions are present[26,36,37], as exhibited in Figure 12. Therefore, the structural hydroxyl groups measured by TGA would not contribute to the measured zeta potential. One potential explanation for the discrepancy in zeta potential is that HMO-2 may have more negative surface functional groups present on its Mn (III) phases. $Mn_8O_{10}Cl_3$ contains oxychloride surface functional groups capable of inner sphere complexation and has been used for nonspecific cation surface sorption in previous literature, suggesting it should exhibit a more negative zeta potential in solution.[56,57]

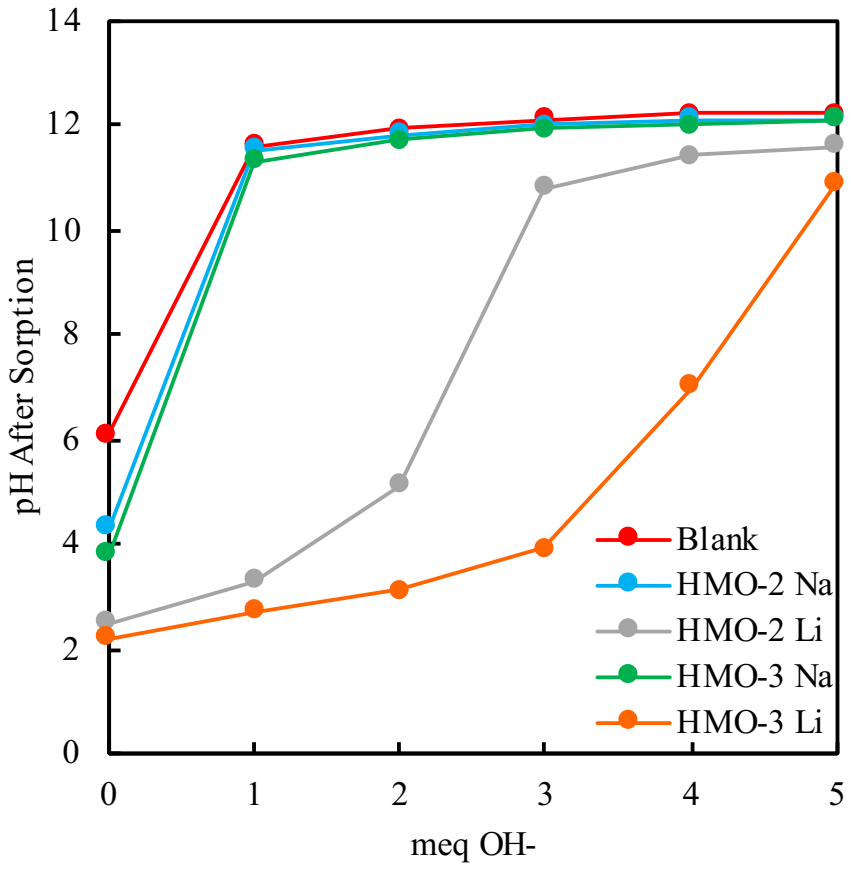

Figure 12: pH buffering ability in Li versus Na containing solutions of HMO-2 and HMO-3.

Data from Li selectivity titrations is shown in Figure 12. For both protonated sorbents, the pH vs. meq OH^- curve under immersion in a NaOH/NaCl solution essentially follows that of the blank titration containing no sorbent. This indicates little or no ion exchange between Na ions in solution and protons in the sorbents.[30,32,33] When immersed in a LiOH/LiCl solution, both sorbents exhibited ion exchange between Li and protons, releasing protons into solution and buffering the pH of the solution.[30,32,33] This experiment verifies that both HMO-2 and HMO-3 are highly Li selective ion exchange sorbents. HMO-3 was able to buffer the solution at higher concentrations of OH^- than HMO-2 due to its higher concentration of ion exchange sites.[30,32,33] The maximum Li uptake by HMO-2 and HMO-3 in these experiments were 18 mg g^{-1} and 27 mg

g^{-1} respectively, without interference from competing cations. These values represent the maximum projected Li sorption capacities which these materials could potentially uptake from FPW. Interestingly, there was an observed production of permanganate from both HMO-2 and HMO-3 in Li titrations in which the final pH was >10, which did not occur in the Na titrations (Figure 13). A similar result was found by Feng *et al*.[33] using a similar experiment. Saenko *et al*.[58] attributed this phenomenon to the redox disproportionation reaction $4Mn^{4+} \rightarrow 3Mn^{3+} + Mn^{7+}$ during lithium sorption, resulting in the release of MnO_4^-.

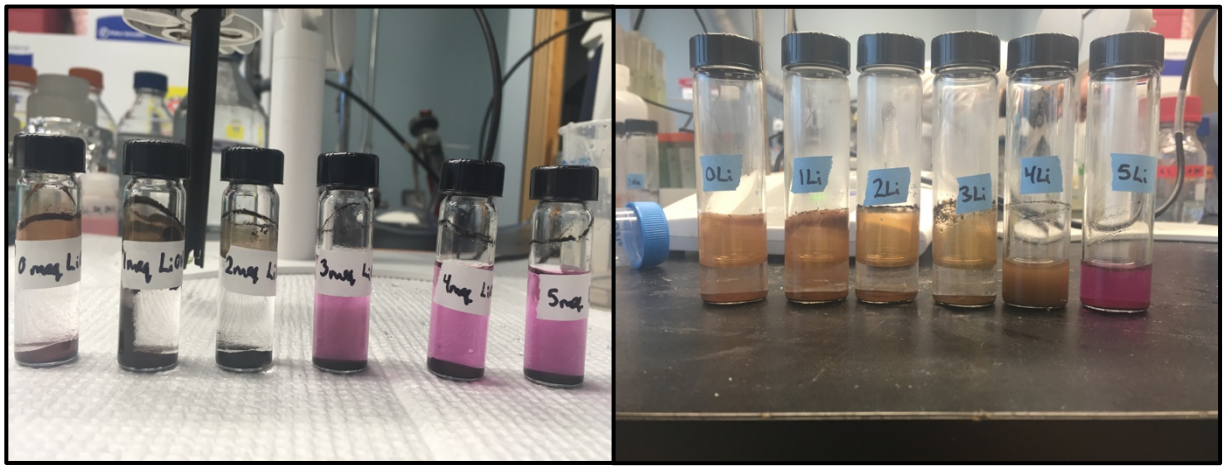

Figure 13: Permanganate formation under alkaline conditions (final pH >10) during lithium containing selectivity titrations with HMO-2 (left) and HMO-3 (right).

3.2. Sorbent Performance in FPW

3.2.1. Optimization of Sorption/Desorption Conditions

The experimental conditions which were tested in this work include sorption pH, sorption temperature and time, sorbent dosage ratio, desorption time and acid concentration. Experimental

conditions were originally optimized using HMO-2, and the same conditions were later applied when using HMO-3 for consistency.

Sorption pH was found to have the most significant impact on both lithium uptake and on the final lithium concentrate purity. Lithium uptake is highly dependent on initial pH due to proton release at ion exchange sites during lithium sorption; this causes the FPW to experience a pH drop over the course of the sorption time.[39] Lithium uptake at an ion exchange site is significantly impeded when solution pH drops below 6.[39] For this reason, in order to maximize lithium recovery, the initial pH of the FPW must be high enough that the majority of the lithium is extracted prior to the solution pH dropping below 6. With an initial sorption pH of 8 and higher, HMO-2 was able to reach its maximum lithium uptake prior to the pH of solution dropping too low for lithium-proton ion exchange (Figure 14). Conversely, an initial pH of 8 and lower resulted in fewer impurities in the final lithium concentrate; at sorption conditions of pH 9 and higher, undesired cations precipitated from solution and were not separated during centrifugation, leading to these impurities being dissolved into the final acid product. This resulted in high Na, Mg and Ca concentrations in the final concentrate for experiments which had an initial pH of 9 and higher (Figure 15). For these reasons, pH 8 was chosen as the optimal sorption pH in this study.

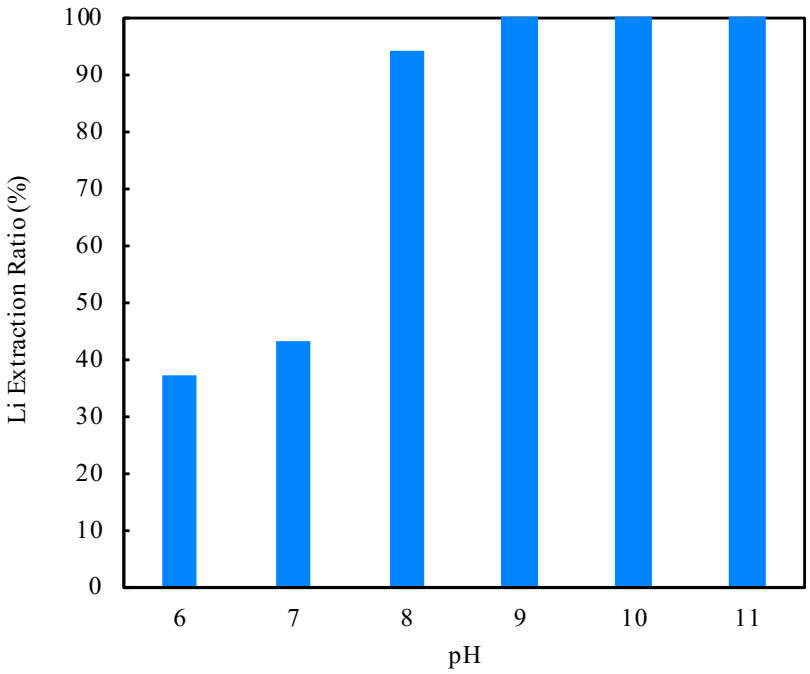

Figure 14: Percent of lithium extracted from FPW at varying initial pH values. Sorption experiments were performed at 70°C for 60 minutes at a sorbent dosage of 5 g L^{-1}.

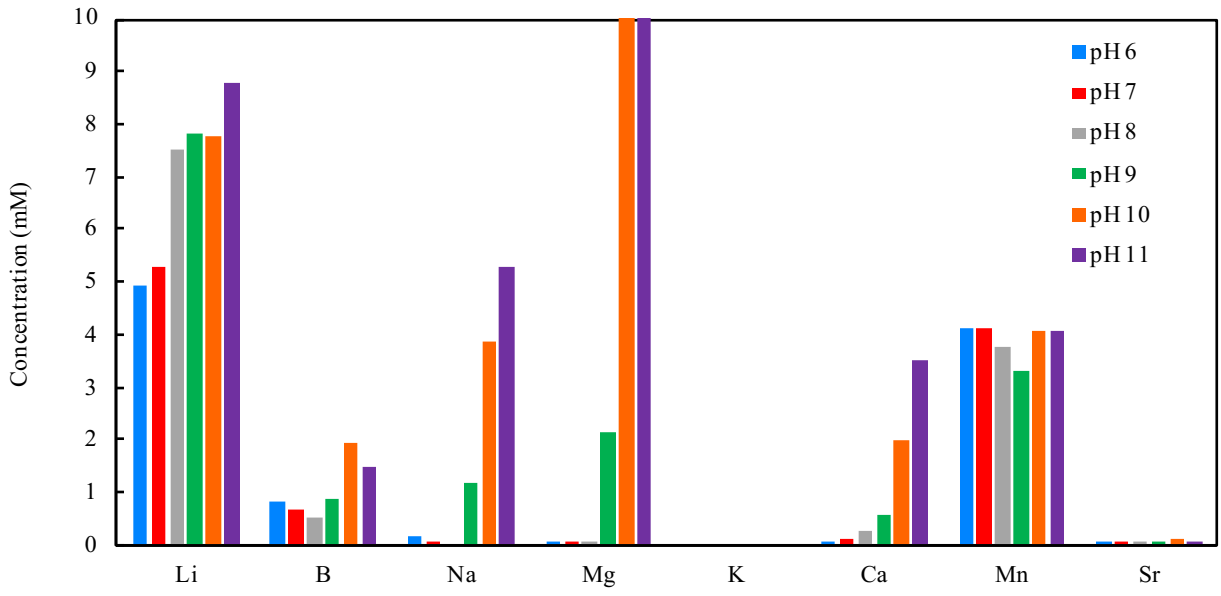

Figure 15: Major ion concentrations in desorption acid after lithium extraction from FPW at varying initial pH values. Desorption experiments were performed in 0.50 M H_2SO_4 at 20°C for 60 minutes.

Two sorption temperatures were tested against one another based on two potential lithium recovery scenarios: lithium sorption directly at the wellhead, and from a storage facility after the FPW has cooled. Temperatures of 70°C (the approximate FPW wellhead temperature) and 20°C were chosen to represent these two scenarios, respectively. It was found that the sorption kinetics and final lithium uptake were highly temperature dependent (Figure 16); at a sorption temperature of 70°C, a maximum lithium uptake of 17 mg g^{-1} was reached in 30 minutes, versus a maximum uptake of 12.5 mg g^{-1} after 4 hours at 20°C.

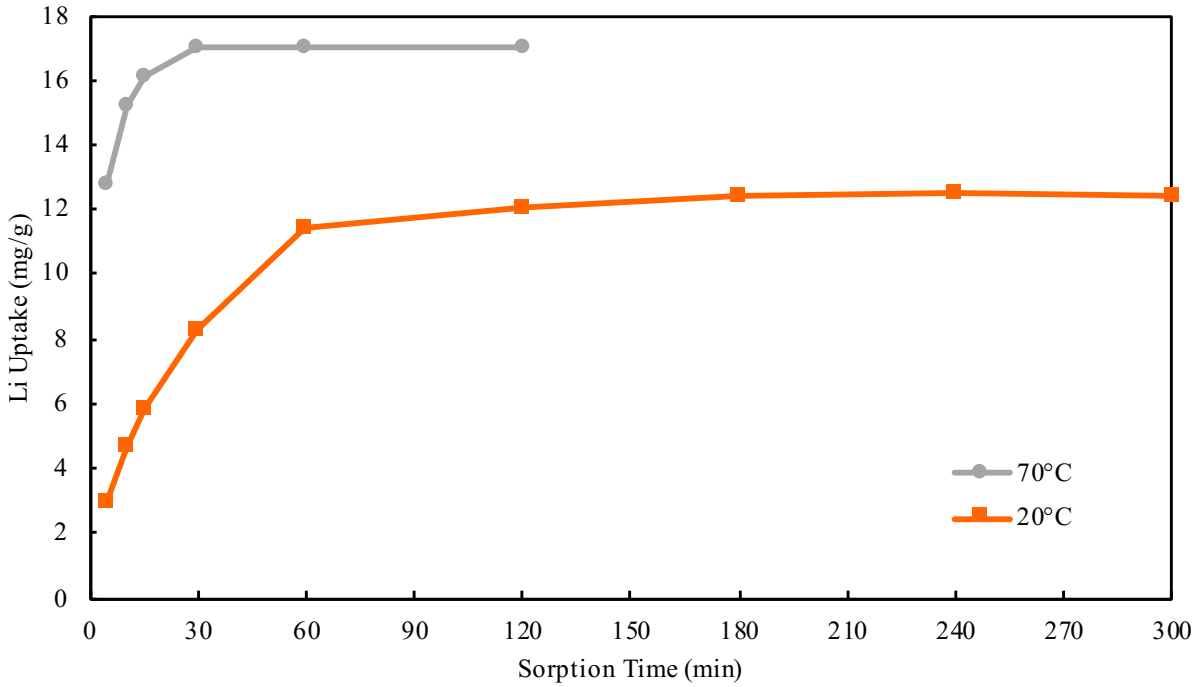

Figure 16: Lithium sorption kinetics at 70°C (the FPW wellhead temperature) and 20°C. These temperatures represent scenarios in which lithium is extracted directly at the wellhead (70°C), or at room temperature after FPW storage (20°C). Sorption experiments were performed using a sorbent dosage of 2.0 g L^{-1}.

Sorbent dosage in the FPW had a significant impact on lithium extraction efficiency and on lithium uptake due to differences in FPW pH drop during sorption (Figure 17, Figure 18). As displayed in Figure 17, higher sorbent dosages of 8.0 g L^{-1} and 4.0 g L^{-1} had relatively high

lithium extraction efficiencies (> 80%), meaning a large fraction of lithium was recovered from solution; however, neither of these experiments resulted in close to 100% lithium recovery, as the FPW pH dropped below 6 before all of the lithium ions could be sorbed from solution (Figure 18). Because of this pH drop, a large number of the ion exchange sites did not sorb lithium and were essentially inactive during these experiments, resulting in low lithium uptakes (on a per mass basis) for these high dosages. Lower sorbent dosages (1.0 and 0.5 mg g^{-1}) resulted in higher lithium uptakes due to the FPW pH remaining high throughout lithium sorption. In these experiments, lithium uptake was near or above the maximum lithium uptake of HMO-2 of 18 mg g^{-1} during the lithium selectivity experiments. These dosages, however, resulted in the sorbent reaching its maximum uptake before the majority of the lithium was removed from solution, leading to the low extraction efficiencies obtained by using 1.0 and 0.5 mg g^{-1} sorbent dosages. For these reasons, a sorbent dosage of 2.0 g L^{-1} was chosen as optimal for these experiments, as it resulted in the best balance between a high lithium extraction efficiency and a high lithium uptake.

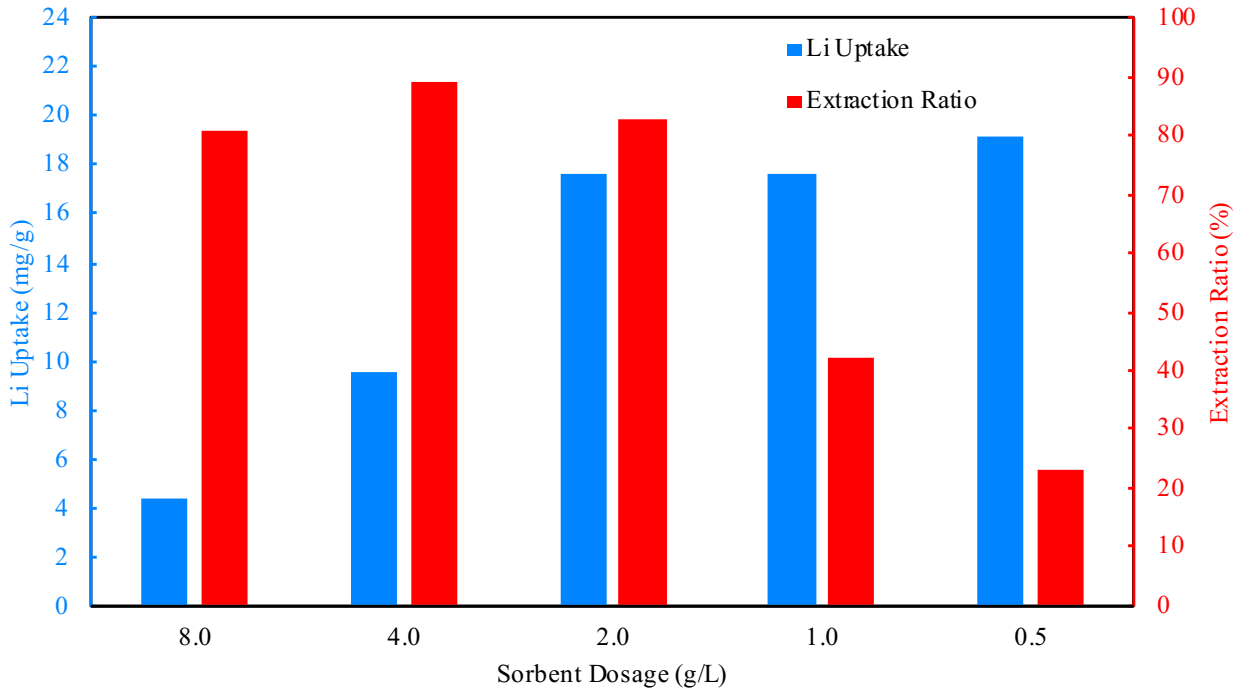

Figure 17: Lithium uptake and lithium extraction efficiency from pH 8 FPW using varying sorbent dosages. Sorption experiments were performed at 70°C for 30 minutes.

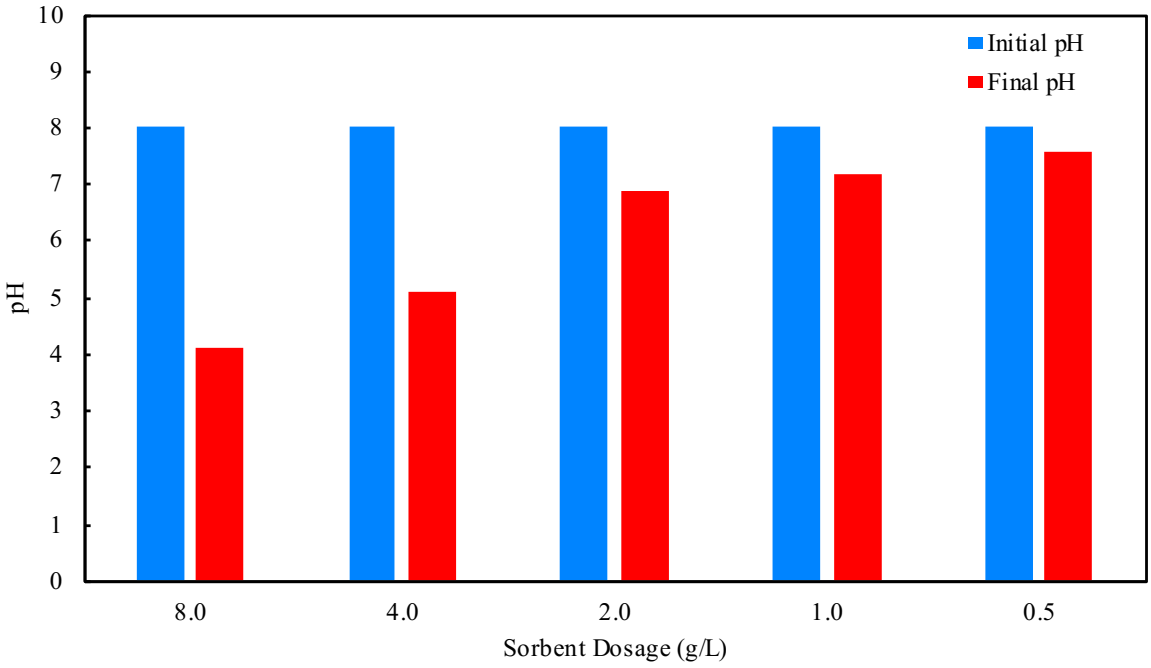

Figure 18: pH drop of FPW after lithium sorption during sorbent dosage optimization experiments (Figure 17).

Desorption performance was less sensitive to the tested conditions as compared to sorption; desorption kinetics were fast, reaching maximum stripping efficiency after 5 minutes (Figure A1), and acid concentration had little effect on stripping efficiency (Figure 19). The exception to this was desorption in 10 mM H_2SO_4; in this experiment, there were fewer total moles of protons in the initial desorption acid than there were total moles of lithium in the sorbent, causing the acid to be completely neutralized prior to complete lithium desorption, as displayed in Figure 19. These desorption experiments utilized a lithium concentration factor (volume ratio of FPW to desorption acid) of 3.0; producing a more concentrated lithium product would require a more concentrated acid in order to avoid neutralization, and so optimal acid concentration would be determined by the desired lithium concentration. Sorbent dissolution in acid was not significantly affected by the tested desorption conditions.

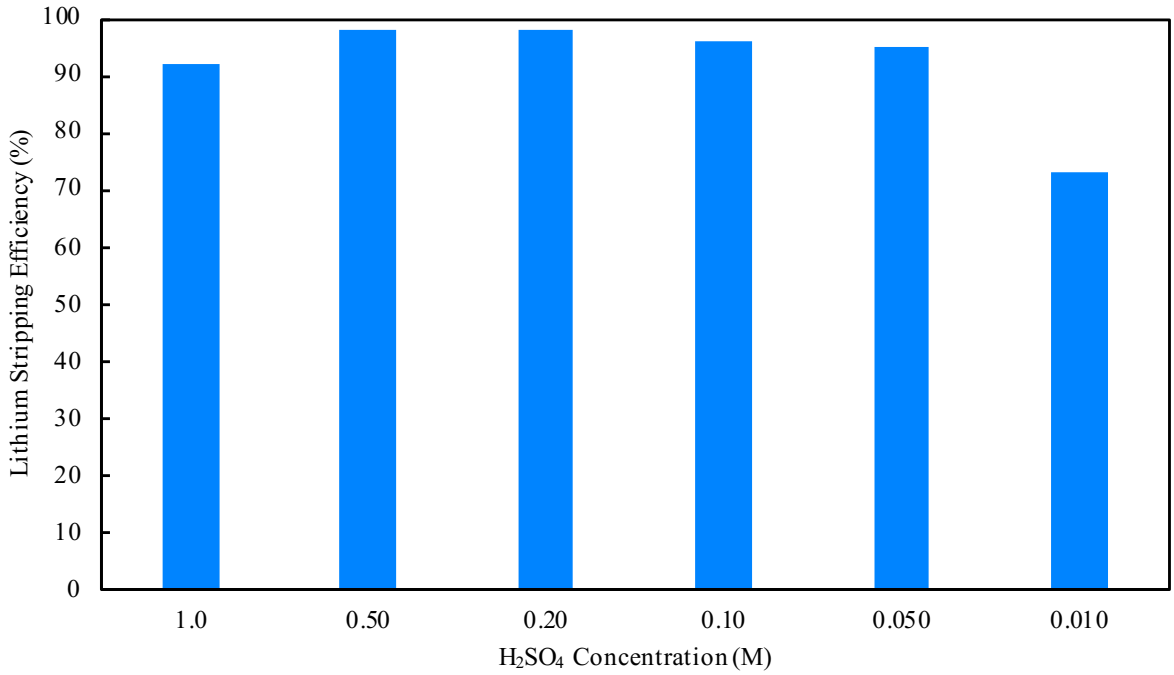

Figure 19: Lithium stripping efficiency during acid desorption in varying concentrations of H_2SO_4. Desorption experiments were performed for 5 minutes at 20°C in a sorbent dosage of 6.0 g L^{-1} following sorption from pH 8 FPW at 70°C for 30 minutes at a sorbent dosage of 2.0 g L^{-1}.

In summary, the optimum lithium recovery conditions were determined to be sorption at pH 8 and 70°C for 30 minutes with a sorbent dosage of 2.0 g L^{-1}, followed by desorption in 0.5 M H_2SO_4 for 5 minutes. At these conditions, HMO-2 was able to extract > 80% of the lithium from the FPW, with an average uptake of 18 mg g^{-1}. Using a concentration factor of 3.0, the lithium stripping efficiency was 98%, leading to a relatively pure acid product containing 15 mmol L^{-1} of lithium (Figure 20). These conditions were used for all lithium sorption and desorption experiments in the following sections.

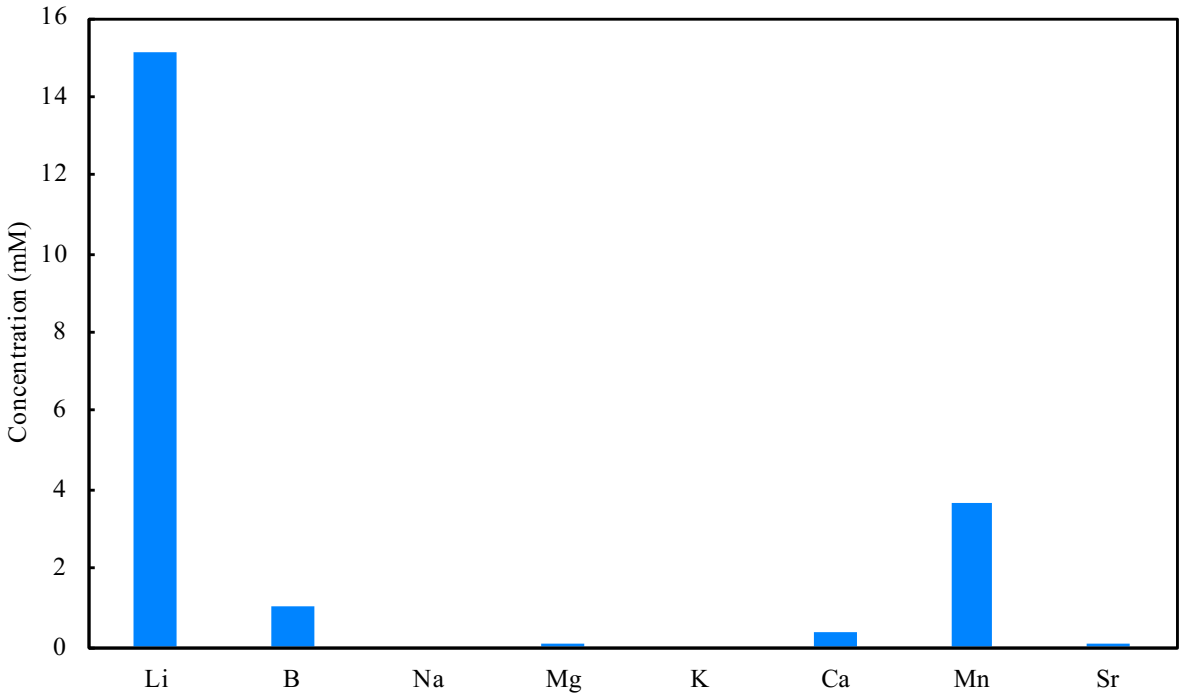

Figure 20: Major cation concentrations in final lithium concentrate after sorption from FPW and desorption in acid under optimized conditions. Sorption was performed from pH 8 FPW at 70°C for 30 minutes at a sorbent dosage of 2.0 g L^{-1}, and desorption was performed in 0.50 M H_2SO_4 for 5 minutes at 20°C in a sorbent dosage of 6.0 g L^{-1}.

3.2.2. Sorption and Desorption Experiments Under Optimized Conditions

Average first cycle lithium uptake from the FPW was comparable between HMO-2 and HMO-3 at approximately 18 mg g^{-1} and 17 mg g^{-1}, respectively. This is consistent with the maximum lithium uptake determined in the selectivity experiments for HMO-2 (18 mg g^{-1}); however, HMO-3 displayed a significantly lower Li uptake from FPW as compared to its maximum uptake of 27 mg g^{-1} determined from the selectivity experiments. This is due to the pH drop of the FPW during lithium sorption as protons were released from ion exchange sites.[39] At an ion exchange site, lithium sorption is significantly impeded when the solution pH drops below 6,[39] and effectively ceases below pH 4,[30] meaning that the maximum uptake capacity cannot be reached if the pH becomes too low during sorption. Experimental conditions were initially optimized for sorption using HMO-2; a higher FPW starting pH would be required for HMO-3 to reach its maximum uptake.

First cycle sorbent loss in acid fluctuated considerably for both sorbents, but was typically between 4-10%. Literature values for sorbent loss during acid desorption from redox-type $LiMn_2O_4$ can be as high as 27%.[59] Pure ion-exchange type $Li_{1.33}Mn_{1.67}O_4$ exhibits far lower sorbent loss because it lacks a reductive manganese dissolution mechanism.[36,40] Manganese dissolution from a pure ion exchange sorbent occurs primarily due to the presence of trace Mn (III) atoms present in the bulk material; the trivalent manganese transfers electrons to Mn (IV) atoms on the particle surface during acid treatment, resulting in the formation and release of Mn (II).[60] Due to this mechanism, pure ion exchange $Li_{1.33}Mn_{1.67}O_4$ and $Li_{1.6}Mn_{1.6}O_4$ sorbents typically experience between 1-2% sorbent loss per cycle.[36,40] Experimental sorbent loss values after sorption from FPW were therefore within a potential range for a sorbent containing redox-

type sorption sites such as HMO-2, but were significantly higher than literature values for a pure ion exchange sorbent such as HMO-3. I therefore speculated that exposure to FPW during lithium sorption leads to an increased sorbent loss in the subsequent desorption step.

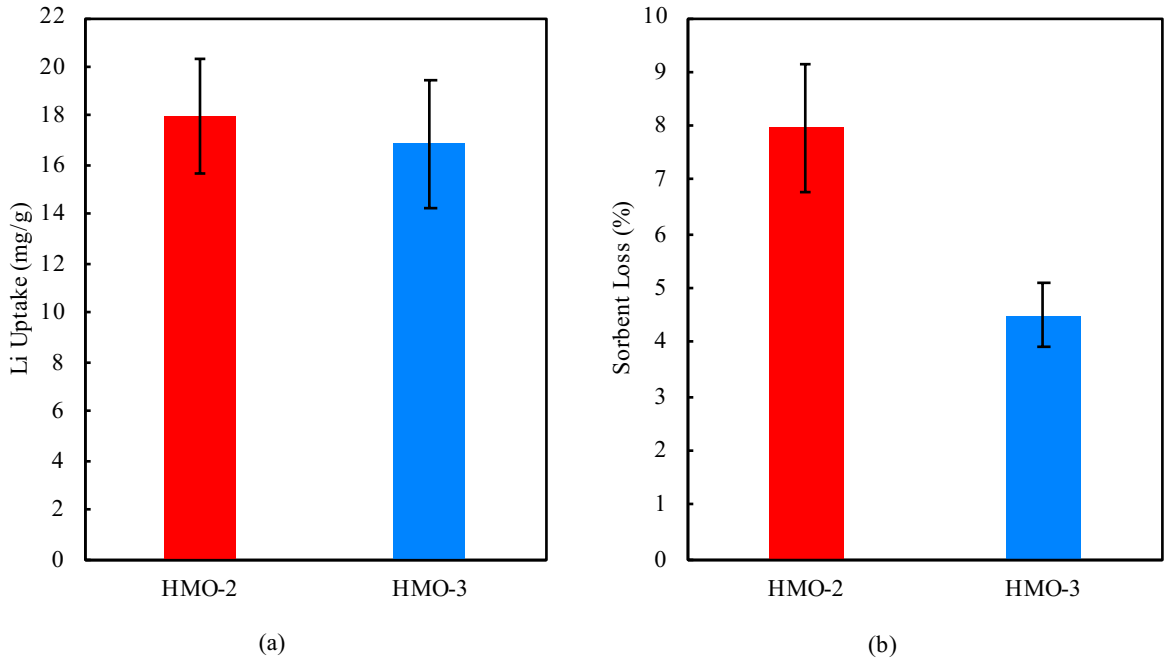

Figure 21: Li uptake (a) and sorbent loss in acid (b) of HMO-2 and HMO-3 during Li recovery from FPW. Error bars represent 1 standard deviation.

3.2.3. Sorbent Recycling

Attempts to recycle spinel lithium manganese oxide sorbents for recovery of lithium from brine have been successful. Tian *et al.*[39] and Ooi *et al.*[37] both found the drop in lithium uptake to be negligible over the course of 5 cycles. Recycling of both HMO-2 and HMO-3 in FPW, however, proved to be challenging in this study. Initial recycle testing was performed on HMO-2, and the methodology which resulted in the most positive outcome was later confirmed to perform similarly on HMO-3.

With no treatment of the FPW, second cycle lithium uptake by HMO-2 dropped significantly to 2 mg g^{-1}, compared to the first cycle Li uptake of 17 mg g^{-1} (Figure A2). On this second sorption cycle, the sorbent was observed to aggregate and float on top of the FPW instead of dispersing as usual. I hypothesized that a coating of non-aqueous organic liquids present in the FPW was formed on the sorbent surface during the first sorption that was carried through the washing and drying process, as reported previously for titanium-based sorbents.[61,62] This hypothesized coating could cause the sorbent to become hydrophobic, reducing its reactive surface area and therefore reducing its sorption capacity. In an attempt to remove any organic coating on the sorbent surface, various organic removal treatments were studied, including removing non aqueous liquids prior to sorption by centrifugation, washing the sorbent with ethanol, washing with hexane, and washing with a surfactant (Figure A2). The most effective of the tested options was washing the sorbent with a surfactant solution (1% Triton) after each sorption cycle prior to the drying step. Using this method, lithium uptake plateaued at 13 mg g^{-1} between cycles 2-5 after a first cycle uptake of 17 mg g^{-1} (Figure 22), indicating that the surfactant was successful in removing the hypothesized organic coating.

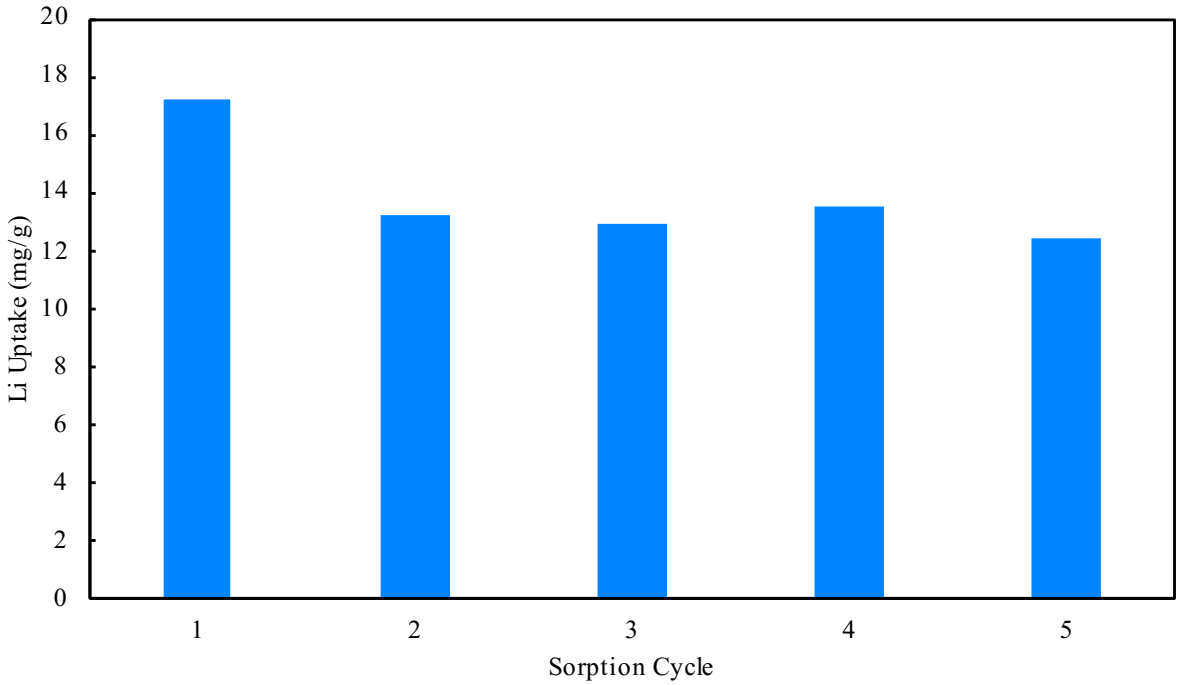

Figure 22: Li uptake when recycling HMO-3 in FPW with a 1% Triton solution wash following each desorption cycle.

3.3. Effect of Organic Compounds on Sorbent Performance and Structure

3.3.1. Sorbent Performance in Synthetic Brine

In order to study the impact of FPW on sorbent loss, a synthetic brine was prepared to replicate the inorganic characteristics of the FPW in the absence of organic compounds. Sorption and desorption experiments were performed on HMO-3 at the previously determined optimized conditions. HMO-3 was used exclusively in these initial experiments due to the large discrepancy between experimental sorbent loss and literature values for similar sorbents.[36,40] Li uptake from the synthetic brine by HMO-3 was slightly higher that from the FPW at 21 mg g^{-1} on average. This is likely due to the synthetic brine having a higher buffering capacity, which limits the pH drop during sorption; the final pH values of the treated fluids were 5.5 and 5.9 for

FPW and synthetic brine, respectively. More significantly, first cycle sorbent loss from HMO-3 was considerably lower with synthetic brine than with FPW at 0.8% on average, which falls within the typical range in literature for sorbent loss from a pure ion exchange sorbent.[36,40] I therefore hypothesized that the organics present in the FPW were reducing Mn (IV) in the sorbent during lithium sorption, leading to a consequent increase of Mn dissolution in acid.

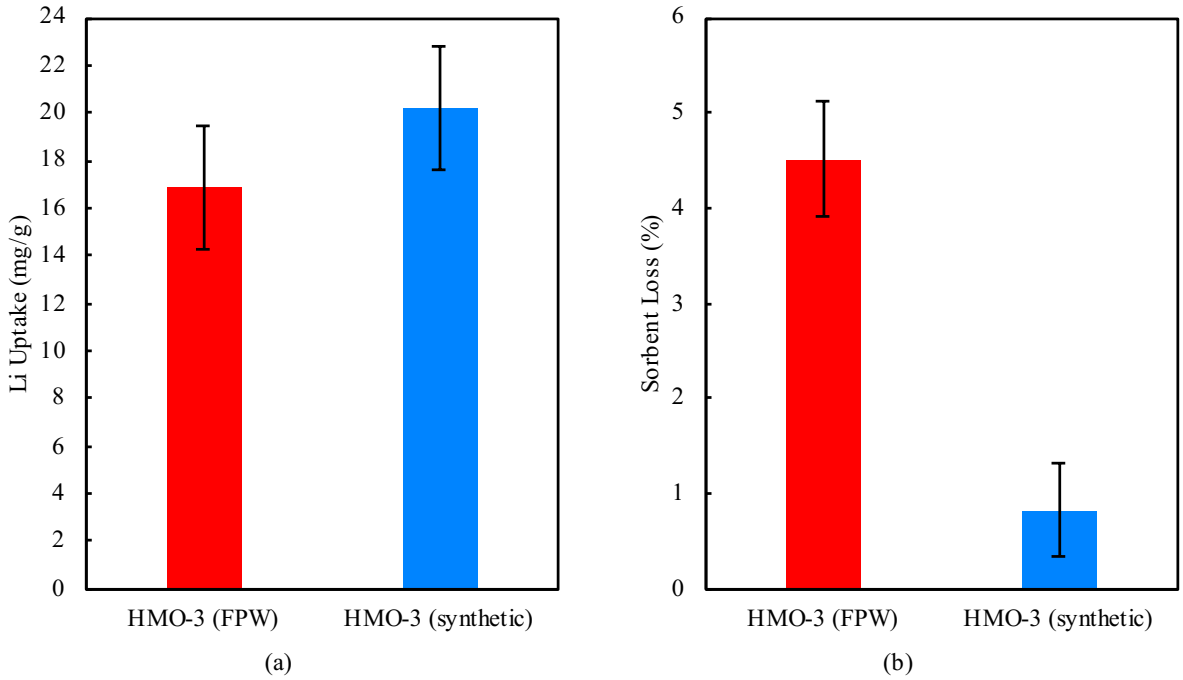

Figure 23: Li uptake (a) and sorbent loss in acid (b) of HMO-3 during Li recovery from FPW and synthetic brine. Error bars represent 1 standard deviation.

3.3.2. Manganese Reduction in FPW

In order to test my hypothesis of Mn reduction by organic compounds, sorption experiments with HMO-2 and HMO-3 were performed in both field collected FPW and synthetic brine, and samples of the sorbents were analyzed after lithium loading and after acid desorption. Z_{Mn} measurements for each experiment are presented in Figure 24.

After both Li loading from synthetic brine and subsequent acid desorption, Z_{Mn} of HMO-3 remains at 4.0, resulting in a low sorbent loss of 0.7% for the cycle. This is due to HMO-3 being an almost exclusively ion exchange sorbent and exhibiting insignificant reductive dissolution in acid.[30-35] Z_{Mn} of HMO-2 drops from 3.64 to 3.59 after Li insertion in synthetic brine due to the presence of redox sites in the sorbent.[30-35] Acid desorption results in a 3.1% sorbent dissolution and a slight increase of Z_{Mn} to 3.61 due to disassociation of the Mn (III) which was produced during Li sorption at redox sites.[30-35]

Both HMO-2 and HMO-3 display a significant drop in Z_{Mn} (0.24 units of Z_{Mn} each) after sorption in the field collected FPW, substantiating the hypothesis of Mn reduction by organics present in the FPW. During subsequent Li desorption in acid, almost all of the Mn which was reduced by the FPW dissolves into solution, resulting in a 9.5% and 10.1% loss of HMO-3 and HMO-2, respectively, and an increase in Z_{Mn} to approximate pre-exposure values for both. This measured Z_{Mn} drop after sorption from FPW is corroborated by XANES data for both sorbents (Table B2).

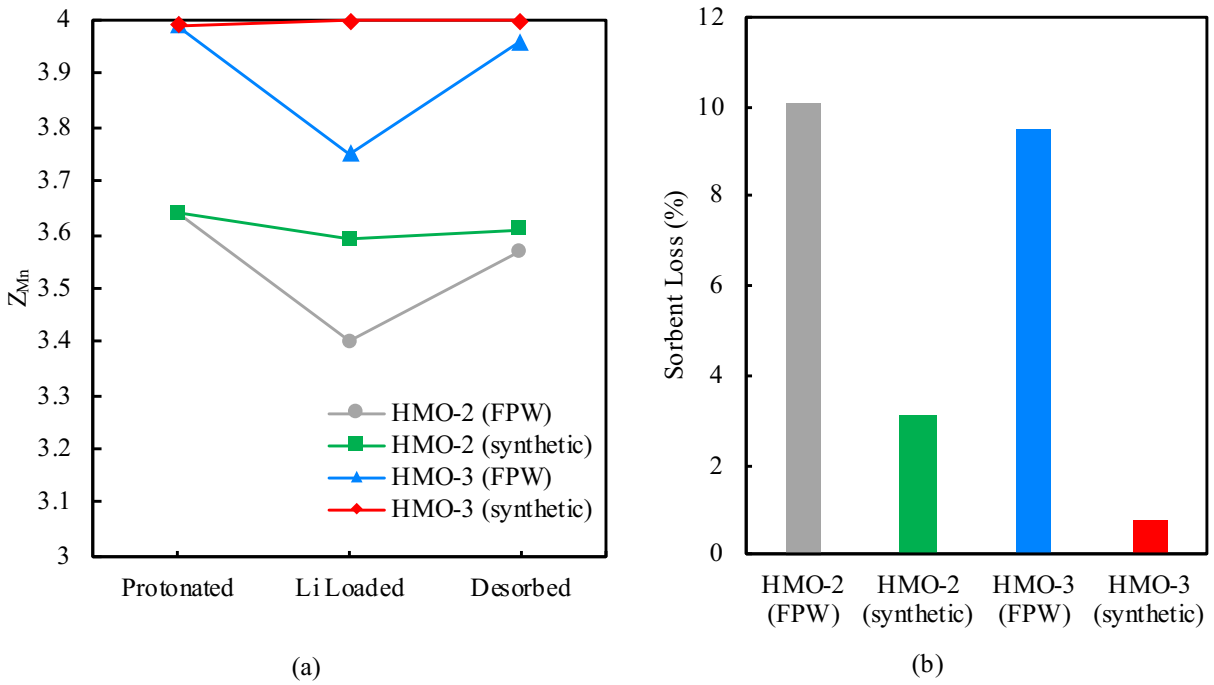

Figure 24: Changes in Z_{Mn} throughout sorption/desorption cycle (a) and resulting sorbent loss in acid (b) of HMO-2 and HMO-3 during Li recovery from both FPW and synthetic brine.

FPW has a highly complex organic profile because it is comprised of components from natural formation water, and additives in the fracturing fluid along with their degradation products.[12,15] A previous study on FPW from the Duvernay formation in Alberta determined that the most common dissolved organic species present were polyethylene glycols (PEGs), octylphenol ethoxylates (OPEs) and alkyl dimethyl benzyl ammonium chlorides (ADBACs).[12] There is an abundance of evidence[63-70] of various easily oxidizable organics reducing manganese oxides in nature. Humic, fulvic, gallic, ascorbic and tannic acids, as well as a wide variety of small aromatic compounds which could be present in FPW, are all able to reduce MnO_x compounds to soluble Mn (II).[63,68] When this occurs, Mn (IV) or Mn (III) is reduced to Mn (II) and is released into solution. This does not appear to be the case during lithium sorption, however, as no measurable Mn was observed in the treated FPW after sorption. The Mn which is

reduced during sorption exists as part of the bulk sorbent, leading to the measured drop in Z_{Mn}. This is further evidenced by the 2nd shell Mn-Mn distances measured by EXAFS (Table B1). In both HMO-2 and HMO-3, the average 2nd shell Mn-Mn distances increase more significantly after lithium sorption from FPW as compared to from synthetic brine. Furthermore, the "lithium loaded from FPW" versions of each sorbent have the widest distribution of Mn-Mn distances (Table B1) compared to any other version of each sorbent. These two pieces of evidence indicate the presence of "fugitive" manganese atoms (bulk Mn atoms which are not part of the spinel structure) in both sorbents after sorption from FPW. These atoms are not part of the crystal structure of the spinel, and would result in different Mn-Mn interatomic distances, thereby causing the larger distribution seen in Table B1. Both of these measurements in both sorbents are comparable to their synthetic brine experiment counterparts post desorption, indicating dissolution of the fugitive manganese atoms in acid.

It is unknown whether the reduced Mn remains as part of the bulk of the sorbent as either Mn (II) or Mn (III), or if it is adsorbed to functional groups on the particle surface and is later released during acid desorption. Saenko *et al*.[58] found that spinel lithium manganese oxides were able to sorb up to 80% of aqueous Mn (II) from an alkali solution; it is therefore possible that the Mn (IV) is being reduced to Mn (II) by organic molecules in the FPW, is released into solution, and is immediately resorbed. XPS results detected only Mn (IV) on the surface of HMO-3 after sorption of lithium from FPW (Table B3); this conflicts with the Mn (II) surface adsorption model, and indicates that the reduced Mn is likely in the bulk of the nanoparticles.

In an attempt to remove redox-active organic molecules, FPW samples were filtered through both a 10 kDa ultrafiltration membrane to remove large organics, and through a 100-250 Da nanofiltration membrane to remove small organics. Ultrafiltration did not significantly impact

the inorganic properties of the FPW; nanofiltration resulted in a 13% decrease in total divalent cations. Properties of the filtered fluids can be referenced in Table 2. After ultrafiltration, the NPOC of the FPW dropped from 180 ppm to 116 ppm, and sorbent loss in acid was not significantly affected. After nanofiltration, the NPOC of the FPW dropped further to 85 ppm, and the sorbent loss in acid after sorption from this fluid dropped to 3.0%. This represents the lowest experimental value recorded for sorbent loss by HMO-3 from the field collected FPW, however, it is still higher than sorbent loss values during lithium recovery from synthetic brine. This suggests that the manganese is being reduced by small organic molecules (< 250 Da) and that complete removal of these organics would lead to sorbent loss values approaching those from the synthetic brine experiments.

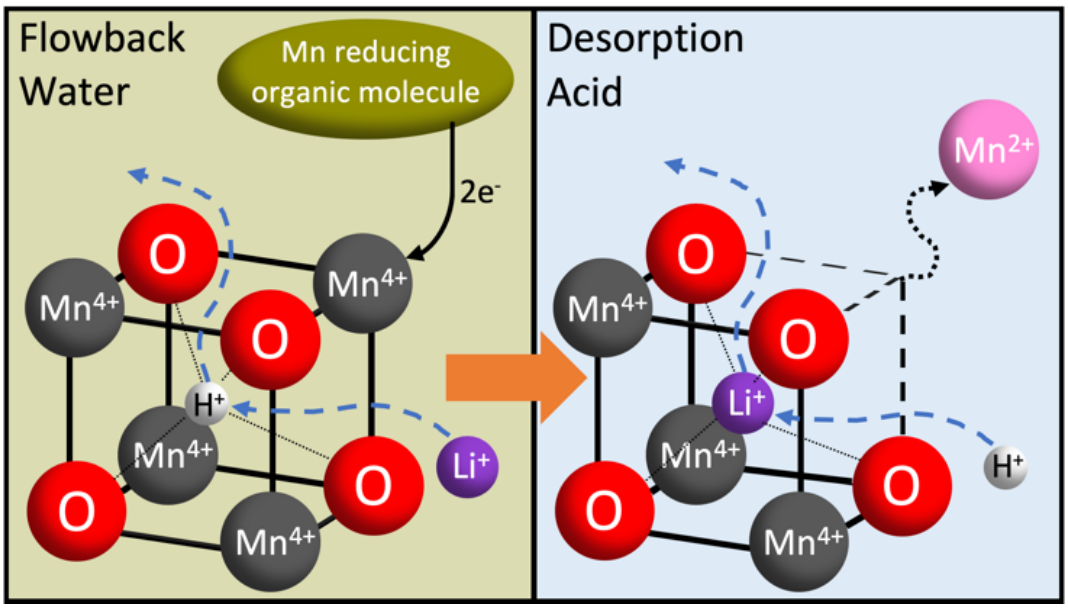

Figure 25: Schematic of proposed mechanism of manganese reductive dissolution by organic molecules.

3.3.3. Effect of Sulfide

Shale gas produced from hot reservoirs can often contain significant levels of hydrogen sulfide.[71] A recent study on FPW originating from the Duvernay formation found a large discrepancy between sulphate and total sulfur concentrations; this suggests that the total sulfide concentrations in the FPW sampled for this study could be as high as 78 ppm.[72] Sulfide concentrations were measured in the FPW used in this work using the Cline Method,[73] and were determined to be negligible. It is important to note, however, that the FPW used in this work was collected in December 2016, and the first lithium recovery experiments were conducted more than a year later, meaning that any sulfides present in the FPW had the opportunity to oxidize due to exposure to atmospheric oxygen during the storage period. Experiments were conducted using HMO-3 in synthetic brine containing 10 ppm and 100 ppm of added sulfide, and resulted in sorbent losses of 2.1% and 8.8% respectively. These results indicate that even low concentrations of sulfide in the FPW lead to increased sorbent loss; therefore, in order for this process to be commercially viable, sulfide would likely have to be removed prior to lithium recovery if present in the FPW of interest.

4. Conclusions

Lithium demand has been increasing dramatically in recent years due mainly to the rise in lithium ion battery production for electric vehicles as the world begins to shift away from fossil fuels and toward renewable sources of energy.[2-6] Currently, the majority of the lithium products produced globally contain lithium sourced from either mineral deposits in Australia, or from high lithium bearing Salars in Chile and other South American countries.[4-6] As the world continues to

shift toward renewable energy and electric vehicle production further increases, lithium supply is likely to represent the rate limiting factor in how quickly lithium ion battery containing electric vehicles can be produced.[7] For this reason, new potential sources of lithium are being explored globally. One potential lithium source exists in the low lithium bearing formation waters of Alberta;[11] although traditionally difficult to access, the hydraulic fracturing water cycle brings this lithium bearing brine to the surface as a waste product, therefore giving the opportunity for lithium recovery from the generated flowback and produced water.[13,14]

In this work, two spinel lithium manganese oxide sorbents were prepared under different conditions using a co-precipitation method. The resulting ionic sieves were characterized for their crystal structure and behavior in solution, and used to recover lithium from FPW originating from the Duvernay formation in Alberta, Canada. I found that in order to achieve a pure ion exchange sorbent without the presence of low valence manganese impurities, a large excess of lithium was required during the synthesis process. The sorbent prepared with a lithium to manganese ratio of 3 contained almost entirely ion exchange lithium sorption sites, and exhibited a higher lithium sorption capacity and a lower sorbent loss during acid desorption than that prepared with a lithium to manganese synthesis ratio of 2. For both materials, sorbent loss in acid was significantly higher after lithium extraction from field collected FPW compared to that after sorption from a synthetic brine. This high sorbent loss was attributed to manganese reduction by dissolved organic molecules in the FPW, which decreased the average valence state of the manganese in the sorbent and led to a subsequent high degree of dissolution of the sorbent in acid. This high sorbent loss presents a significant barrier to commercialization of this technology, as recycling of the sorbent would be essential to the economic viability of this process if applied in the future. Partial removal of these organics using nanofiltration presented

positive results, significantly reducing the degree of sorbent loss. It is expected that complete removal of organics from the FPW would yield sorbent loss results similar to those found during lithium recovery from synthetic brine; this would additionally improve recyclability by removing the need for a post-desorption surfactant wash.

5. Future Work

Based on the experiments conducted in this work, several aspects of lithium recovery from FPW using a manganese-based sorbent should be further investigated. Recommendations for future work are listed below:

1. As a continuation of the current study, I plan to use transmission electron microscopy in conjunction with electron energy loss spectroscopy (TEM-EELS) in order to map the average manganese valence across individual particles on the sub-nanometer scale. Using this method, I will be able to determine the spatial distribution of manganese valence within each particle. I hope that this will bring some clarity as to why the bulk Z_{Mn} of HMO-3 dropped to 3.75 after lithium loading from FPW, while no Mn (III) was detected on its surface using XPS. I hypothesized that an oxidized layer of Mn (IV) could have formed on the surface of the particles after drying and storage, and that the majority of the Mn (III) is therefore in the bulk of the particle. If this was the case, it is likely that manganese reduction by organics is not simply a surface phenomenon. I hope that by showing where in the particle the reduced manganese exists (surface vs. bulk), TEM-EELS could begin to reveal the mechanism for manganese reduction by organics. If TEM-EELS is unsuccessful at providing a mechanism for Mn reduction, other methods

such as measurement of Mn stable isotopes, may be used as a tracer to track Mn loss from the sorbent.

2. Pretreatment of the FPW should be further studied in order to remove manganese-reducing organics. Furthermore, the organic profile of the FPW should be further studied in order to determine which class(es) of organic molecules are responsible for manganese reduction, and therefore which are most essential to remove. Methods such as oxidation, nanofiltration, and removal using materials which bind to organic molecules (such as activated carbon and organoclay) would be some potential pretreatment methods. Such research is essential to this technology in order to minimize sorbent loss in acid, and to improve recyclability of the sorbent without the need for a surfactant wash.

3. Hydrogen sulfide concentrations in the FPW should be measured at wellhead conditions. If significant levels of sulfide are measured, sulfide removal technologies (such as oxidation) should be investigated.

4. This work used FPW from only a single well collected at a single time. This technology should be implemented at the laboratory scale on other FPW samples in order to determine FPW characteristics (concentrations of various cations, organic molecules, buffering capacity, wellhead temperature, etc.) to which lithium recovery is most sensitive. In order to achieve this, the optimization process described in this work should be carried out on various other lithium bearing FPW samples.

5. This work describes lithium recovery using a manganese-based sorbent at the laboratory scale only. If this technology were to be further researched for commercial scale use,

scaled up experiments using this technology would be required. Such a study should research different reactor designs which could carry out the lithium recovery process described in this work, as well as address various issues which come with industrialization of a laboratory scale process. Potential reactor designs could include fluidized bed reactors, batch reactors, or sorption columns. In order to facilitate the separation of the nanoparticles after each step, plating the nanoparticles onto a surface or pressing them into beads may be necessary.

6. If this process were to be commercialized in the future, a full economic analysis of a scaled up version of this process would have to be conducted in order to determine the best way to make it economically viable.

References

1. Meng, F.; McNeice, J.; Zadeh, S. S.; Ghahreman, A. Review of Lithium Production and Recovery from Minerals, Brines, and Lithium-Ion Batteries. *Miner. Process. Extr. M.* **2019**, 1-19.

2. Swain, B. Separation and purification of lithium by solvent extraction and supported liquid membrane, analysis of their mechanism: a review. *J. Chem. Technol. & Biotechnol*. **2016**, *91*, 2549-2562.

3. Martin, G.; Rentsch, L.; Höck, M.; & Bertau, M. Lithium market research–global supply, future demand and price development. *Energy Storage Mater.* **2017**, *6*, 171-179.

4. Jaskula, B.W. *Mineral Commodity Summaries Lithium*; U.S. Geological Survey: Reston, VA, 2019; pp 98-99.

5. Jaskula, B.W. *Mineral Commodity Summaries Lithium*; U.S. Geological Survey: Reston, VA, 2020; pp 98-99.

6. Jaskula, B.W. *Mineral Commodity Summaries Lithium*; U.S. Geological Survey: Reston, VA, 2018; pp 98-99.

7. Speirs, J.; Contestabile, M.; Houari, Y.; Gross, R. The future of lithium availability for electric vehicle batteries. *Renew. Sust. Energ. Rev*. **2014**, *35*, 183-193.

8. U.S. Geological Survey. *Mineral Commodity Summaries 2019*; U.S. Geological Survey: Reston, VA, 2019; pp 6.

9. Kavanagh, L.; Keohane, J.; Garcia Cabellos, G.; Lloyd, A.; Cleary, J. Global lithium sources—industrial use and future in the electric vehicle industry: a review. *Resources* **2018**, *7*, 57.

10. U.S. Geological Survey. *Mineral Commodity Summaries 2020*; U.S. Geological Survey: Reston, VA, 2020; pp 195-196.

11. Eccles, D.R.; Berhane, H. *Geological introduction to lithium-rich formation water with emphasis on the Fox Creek area of west-central Alberta (NTS 83F and 83K)*; Energy Resources Conservation Board, Edmonton, AB, 2011; pp 1-17.

12. Zhong, C.; Li, J.; Flynn, S. L.; Nesbø, C. L.; Sun, C.; von Gunten, K.; Lanoil, B.D.; Goss G.G.; Martin, J.W.; Alessi, D. S. Temporal Changes in Microbial Community Composition and Geochemistry in Flowback and Produced Water from the Duvernay Formation. *ACS Earth Space Chem.* **2019**, *3*, 1047-1057.

13. Jang, Y.; & Chung, E. Adsorption of lithium from shale gas produced water using titanium based adsorbent. *Ind. Eng. Chem. Res.* **2018**, *57*, 8381-8387.

14. Jang, E.; Jang, Y.; Chung, E. Lithium recovery from shale gas produced water using solvent extraction. *Appl. Geochem.* **2017**, *78*, 343-350.

15. He, Y.; Flynn, S. L.; Folkerts, E. J.; Zhang, Y.; Ruan, D.; Alessi, D. S.; Martin, J. W.; Goss, G. G. Chemical and Toxicological Characterizations of Hydraulic Fracturing Flowback and Produced Water. *Water Res.* **2017**, 114, 78−87.

16. Barati, R.; & Liang, J. T. A review of fracturing fluid systems used for hydraulic fracturing of oil and gas wells. *J. Appl. Polym. Sci.* **2014**, *131*, 40735.

17. Shaffer, D. L.; Arias Chavez, L. H.; Ben-Sasson, M.; Romero-Vargas Castrillón, S.; Yip, N. Y.; Elimelech, M. Desalination and reuse of high-salinity shale gas produced water: drivers, technologies, and future directions. *Environ. Sci. Technol.* **2013**, *47*, 9569-9583.

18. U.S. Environmental Protection Agency. The Hydraulic Fracturing Water Cycle. https://www.epa.gov/hfstudy/hydraulic-fracturing-water-cycle (accessed June 15, 2020).

19. Flexer, V.; Baspineiro, C. F.; Galli, C. I. Lithium recovery from brines: A vital raw material for green energies with a potential environmental impact in its mining and processing. *Sci. Total Environ.* **2018**, *639*, 1188-1204.

20. Zhang, Y.; Hu, Y.; Wang, L.; Sun, W. Systematic review of lithium extraction from salt-lake brines via precipitation approaches. *Miner. Eng.* **2019**, *139*, 105868.

21. Hano, T.; Matsumoto, M.; Ohtake, T.; Egashir, N.; Hori, F. Recovery of lithium from geothermal water by solvent extraction technique. *Solvent Extr. Ion Exc.* **1992**, *10*, 195-206.

22. Goodenough, R.D.; Remigius, A.G. Extraction of lithium halides from calcium-containing brines in the presence of urea and alcohol-ketone. U.S. Patent 3,306,712, Feb. 28, 1967.

23. Kanoh, H.; Ooi, K.; Miyai, Y.; Katoh, S. Electrochemical recovery of lithium ions in the aqueous phase. *Sep. Sci. Tech.* **1993**, *28*, 643-651.

24. Kim, S.; Lee, J.; Kang, J. S.; Jo, K.; Kim, S.; Sung, Y. E.; Yoon, J. Lithium recovery from brine using a λ-MnO2/activated carbon hybrid supercapacitor system. *Chemosphere* **2015**, *125*, 50-56.

25. Lin, H.; Yu, X.; Li, M.; Duo, J.; Guo, Y.; Deng, T. Synthesis of Polyporous Ion-Sieve and Its Application for Selective Recovery of Lithium from Geothermal Water. *ACS Appl. Mater. Interfaces* **2019**, *11*, 26364-26372.

26. Xu, X.; Chen, Y.; Wan, P.; Gasem, K.; Wang, K.; He, T.; Adidharma, H.; Fan, M. Extraction of lithium with functionalized lithium ion-sieves. *Prog. Mater. Sci.* **2016**, *84*, 276-313.

27. Ji, Zhi-Yong; Zhao, Meng-Yao; Yuan, Jun-Sheng; Wang, Jun; Zhou, Jun-Qi; Yin, Heng-Bo; Sun, Bu-Yun. Li^+ Extraction from Spinel-Type $LiMn_2O_4$ in Different Eluents and Li^+ Insertion in the Aqueous Phase. *Solvent Extr. Ion Exc.* **2016**, *34,* 549-557.

28. Meshram, P.; Pandey, B. D.; Mankhand, T. R. Extraction of lithium from primary and secondary sources by pre-treatment, leaching and separation: A comprehensive review. *Hydrometallurgy* **2014**, *150*, 192-208.

29. Swain, B. Recovery and recycling of lithium: A review. *Sep. Purif. Technol.* **2017**, *172*, 388-403.

30. Feng, Q.; Miyai, Y.; Kanoh, H.; Ooi, K. Li^+ extraction/insertion with spinel-type lithium manganese oxides. Characterization of redox-type and ion-exchange-type sites. *Langmuir* **1992**, *8*, 1861-1867.

31. Wang, L.; Ma, W.; Liu, R.; Li, H. Y.; Meng, C. G. Correlation between Li^+ adsorption capacity and the preparation conditions of spinel lithium manganese precursor. *Solid State Ionics* **2006**, *177*, 1421-1428.

32. Ooi, K., Miyai, Y., & Sakakihara, J. Mechanism of Li^+ insertion in spinel-type manganese oxide. Redox and ion-exchange reactions. *Langmuir* **1991**, *7*, 1167-1171.

33. Feng, Q.; Kanoh, H.; Miyai, Y.; Ooi, K. Hydrothermal synthesis of lithium and sodium manganese oxides and their metal ion extraction/insertion reactions. *Chem. Mater.* **1995**, *7*, 1226-1232.

34. Sato, K.; Poojary, D. M.; Clearfield, A.; Kohno, M.; Inoue, Y. The surface structure of the proton-exchanged lithium manganese oxide spinels and their lithium-ion sieve properties. *J. Solid State Chem.* **1997**, *131*, 84-93.

35. Feng, Q.; Kanoh, H.; Ooi, K. Manganese oxide porous crystals. *J. Mater. Chem.* **1999**, *9*, 319-333.

36. Chitrakar, R.; Kanoh, H.; Miyai, Y.; Ooi, K. Recovery of lithium from seawater using manganese oxide adsorbent ($H_{1.6}Mn_{1.6}O_4$) derived from $Li_{1.6}Mn_{1.6}O_4$. *Ind. Eng. Chem. Res.* **2001**, *40*, 2054-2058.

37. Ooi, K.; Miyai, Y.; Katoh, S. Recovery of lithium from seawater by manganese oxide adsorbent. *Sep. Sci. Technol*. **1986**, *21*, 755-766.

38. Chitrakar, R.; Kanoh, H.; Miyai, Y.; Ooi, K. A New Type of Manganese Oxide (MnO_2•0.5 H_2O) Derived from $Li_{1.6}Mn_{1.6}O_4$ and Its Lithium Ion-Sieve Properties. *Chem. Mater.* **2000**, *12*, 3151-3157.

39. Tian, L.; Ma, W.; Han, M. Adsorption behavior of Li^+ onto nano-lithium ion sieve from hybrid magnesium/lithium manganese oxide. *Chem. Eng. J.* **2010**, *156*, 134-140.

40. Xiao, J.; Nie, X.; Sun, S.; Song, X.; Li, P.; Yu, J. Lithium ion adsorption–desorption properties on spinel $Li_4Mn_5O_{12}$ and pH-dependent ion-exchange model. *Adv. Powder Technol.* **2015**, *26*, 589-594.

41. Umeno, A.; Miyai, Y.; Takagi, N.; Chitrakar, R.; Sakane, K.; Ooi, K. Preparation and adsorptive properties of membrane-type adsorbents for lithium recovery from seawater. *Ind. Eng. Chem Res.* **2002**, *41*, 4281-4287.

42. Zandevakili, S.; Ranjbar, M.; Ehteshamzadeh, M. Recovery of lithium from Urmia Lake by a nanostructure MnO2 ion sieve. *Hydrometallurgy* **2014**, *149*, 148-152.

43. Freeman, D. S.; Chapman, W. G. An improved oxalate method for the determination of active oxygen in manganese dioxide. *Analyst* **1971**, *96*, 865-869.

44. House, R. A.; Maitra, U.; Jin, L.; Lozano, J. G.; Somerville, J. W.; Rees, N. H.; Naydlor, A.J.; Duda, L.C.; Massel, F.; Chadwick, A.V.; Ramos, S.; Pickup, D.M.; McNally D.E.; Lu, X; Schmitt, T; Roberts, M.R.; Bruce, P.G. What triggers oxygen loss in oxygen redox cathode materials? *Chem. Mater.* **2019**, *31*, 3293-3300.

45. McLeod, L. K.; Spikes, G. H.; Kashtiban, R. J.; Walker, M.; Chadwick, A. V.; Sharman, J. D.; Walton, R. I. Structures of mixed manganese ruthenium oxides $(Mn_{1-x}Ru_x)O_2$ crystallised under acidic hydrothermal conditions. *Dalton Trans.* **2020**, *49*, 2661-2670.

46. Ravel, B.; Newville, M. ATHENA, ARTEMIS, HEPHAESTUS: data analysis for X-ray absorption spectroscopy using IFEFFIT. *J. Synchrotron Radiat.* **2005**, *12*, 537-541.

47. Cerrato, J. M.; Hochella Jr, M. F.; Knocke, W. R.; Dietrich, A. M.; Cromer, T. F. Use of XPS to identify the oxidation state of Mn in solid surfaces of filtration media oxide samples from drinking water treatment plants. *Environ. Sci. Technol.* **2010**, *44*, 5881-5886.

48. Brunauer, S.; Emmett, P. H.; Teller, E. Adsorption of gases in multimolecular layers. *J. Am. Chem. Soc.* **1938**, *60*, 309-319.

49. Ammundsen, B.; Aitchison, P. B.; Burns, G. R.; Jones, D. J.; Rozière, J. Proton insertion and lithium-proton exchange in spinel lithium manganates. *Solid State Ionics* **1997**, *97*, 269-276.

50. Euzen, P.; Leone, P.; Palvadeau, P.; Queignec, M.; Rouxel, J. Synthesis and structural studies of manganese oxyhalides with a multisite framework: Part one: $Mn_8O_{10}Cl_3$. *Mater. Res. Bull.* **1992**, *27*, 1295-1300.

51. Aitchison, P.; Ammundsen, B.; Rozière, J.; Burns, G. R.; Jones, D. J. Local structure and lithium-proton ion exchange in $Li_{1.33-x/3}Co_xMn_{1.67-2x/3}O_4$ spinels. *Solid State Ionics* **2005**, *176*, 813-821.

52. Ammundsen, B.; Jones, D. J.; Rozière, J.; Burns, G. R. Effect of chemical extraction of lithium on the local structure of spinel lithium manganese oxides determined by X-ray absorption spectroscopy. *Chem. Mater.* **1996**, *8*, 2799-2808.

53. Ariza, M. J.; Jones, D. J.; Rozière, J.; Chitrakar, R.; Ooi, K. Probing the local structure and the role of protons in lithium sorption processes of a new lithium-rich manganese oxide. *Chem. Mater.* **2006**, *18*, 1885-1890.

54. Tang, W.; Kanoh, H.; Yang, X.; Ooi, K. Preparation of plate-form manganese oxide by selective lithium extraction from monoclinic Li_2MnO_3 under hydrothermal conditions. *Chem. Mater.* **2000**, *12*, 3271-3279.

55. Li, Y.; Bian, Y.; Qin, H.; Zhang, Y.; Bian, Z. Photocatalytic reduction behavior of hexavalent chromium on hydroxyl modified titanium dioxide. *Appl. Catal., B* **2017**, *206*, 293-299.

56. Krauklis, A.; Ozola, R.; Burlakovs, J.; Rugele, K.; Kirillov, K.; Trubaca-Boginska, A.; Rubenis, K; Stepanova, V.; Klavins, M. FeOOH and $Mn_8O_{10}Cl_3$ modified zeolites for As (V) removal in aqueous medium. *J. Chem. Technol. Biotechnol.* **2017**, *92*, 1948-1960.

57. Halevas, E.; Malakopoulos, A.; Delimitis, A.; Zaspalis, V.; Litsardakis, G.; Salifoglou, A. Manganese Oxychloride-Modified Hydrophobic Silica Targets Removal of Nitrates from Water. *Water, Air, Soil Pollut.* **2013**, *224*, 1598.

58. Saenko, E. V.; Leont'eva, G. V.; Vol'khin, V. V.; Kolyshkin, A. S. Variation of the composition and properties of lithium manganese oxide spinel in lithiation-delithiation cycles. *Russ. J. Inorg. Chem.* **2007**, *52*, 1312-1316.

59. Ooi, Kenta; Miyai, Yoshitaka; Katoh, Shunsaku; Maeda, Hiroshi; Abe, Mitsuo. Lithium-ion Insertion/Extraction Reaction with λ-MnO_2 in the Aqueous Phase. *Chem. Lett.* **1988**, *17,* 989-992.

60. Gao, A.; Sun, Z.; Li, S.; Hou, X.; Li, H.; Wu, Q.; Xi, X. The mechanism of manganese dissolution on $Li_{1.6}Mn_{1.6}O_4$ ion sieves with HCl. *Dalton Trans.* **2018**, *47*, 3864-3871.

61. Jang, Y.; Chung, E. Influence of Alkanes on Lithium Adsorption and Desorption of a H_2TiO_3 Ion Sieve Adsorbent in Synthetic Shale Gas-Produced Water. *Ind. Eng. Chem. Res.* **2019**, *58*, 21897-21903.

62. Jang, Y.; Chung, E. Lithium adsorptive properties of H_2TiO_3 adsorbent from shale gas produced water containing organic compounds. *Chemosphere* **2019**, *221*, 75-80.

63. Stone, A. T.; Morgan, J. J. Reduction and dissolution of manganese (III) and manganese (IV) oxides by organics: 2. Survey of the reactivity of organics. *Environ. Sci. Technol.* **1984**, *18*, 617-624.

64. Canfield, D. E.; Thamdrup, B.; Hansen, J. W. The anaerobic degradation of organic matter in Danish coastal sediments: iron reduction, manganese reduction, and sulfate reduction. *Geochim. Cosmochim. Acta* **1993**, *57*, 3867-3883.

65. Stone, A. T.; Morgan, J. J. Reduction and dissolution of manganese (III) and manganese (IV) oxides by organics. 1. Reaction with hydroquinone. *Environ. Sci. Technol.* **1984**, *18*, 450-456.

66. Okita, P. M.; Maynard, J. B.; Spiker, E. C.; Force, E. R. Isotopic evidence for organic matter oxidation by manganese reduction in the formation of stratiform manganese carbonate ore. *Geochim. Cosmochim. Acta* **1988**, *52*, 2679-2685.

67. Burdige, D. J. The biogeochemistry of manganese and iron reduction in marine sediments. *Earth-Sci. Rev.* **1993**, *35*, 249-284.

68. Sunda, W. G.; Huntsman, S. A.; Harvey, G. R. Photoreduction of manganese oxides in seawater and its geochemical and biological implications. *Nature* **1983**, *301*, 234-236.

69. Sunda, W. G.; Huntsman, S. A. Photoreduction of manganese oxides in seawater. *Mar. Chem.* **1994**, *46*, 133-152.

70. Crerar, D. A.; DA, C.; RK, C.; HL, B. Organic controls on the sedimentary geochemistry of manganese. *Acta Mineral.-Petrogr., Szeged* **1972**, *20*, 217-226.

71. Pirzadeh, P.; Lesage, K. L.; Marriott, R. A. Hydraulic fracturing additives and the delayed onset of hydrogen sulfide in shale gas. *Energy Fuels* **2014**, *28*, 4993-5001.

72. Flynn, S. L.; von Gunten, K.; Warchola, T.; Snihur, K.; Forbes, T. Z.; Goss, G. G.; Gingras, M.K.; Konhauser, K.O.; Alessi, D. S. Characterization and implications of solids associated with hydraulic fracturing flowback and produced water from the Duvernay Formation, Alberta, Canada. *Environ. Sci.: Process. Impacts* **2019**, *21*, 242-255.

73. Cline, J. D. Spectrophotometric determination of hydrogen sulfide in natural waters 1. *Limnol. Oceanogr.* **1969**, *14*, 454-458.

Appendix A: Optimization of Sorption/Desorption Conditions

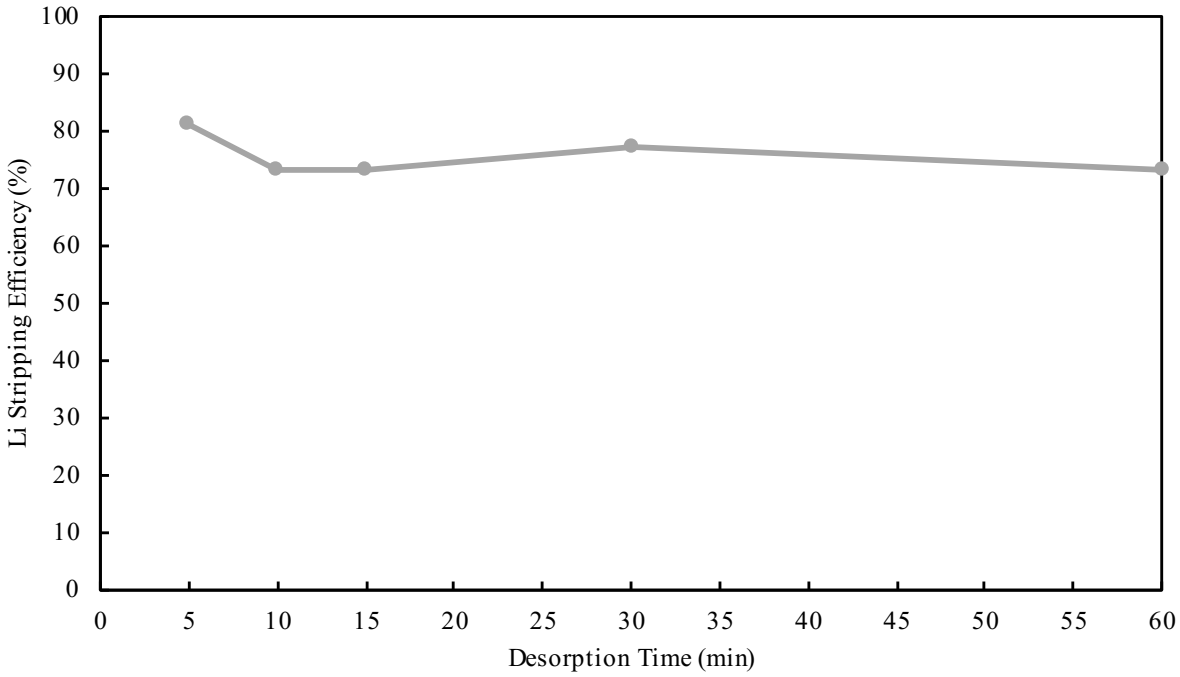

Figure A1: Lithium desorption kinetics. Experiment was performed in 0.50 M H_2SO_4 at 20°C in a sorbent dosage of 6.0 g L^{-1}.

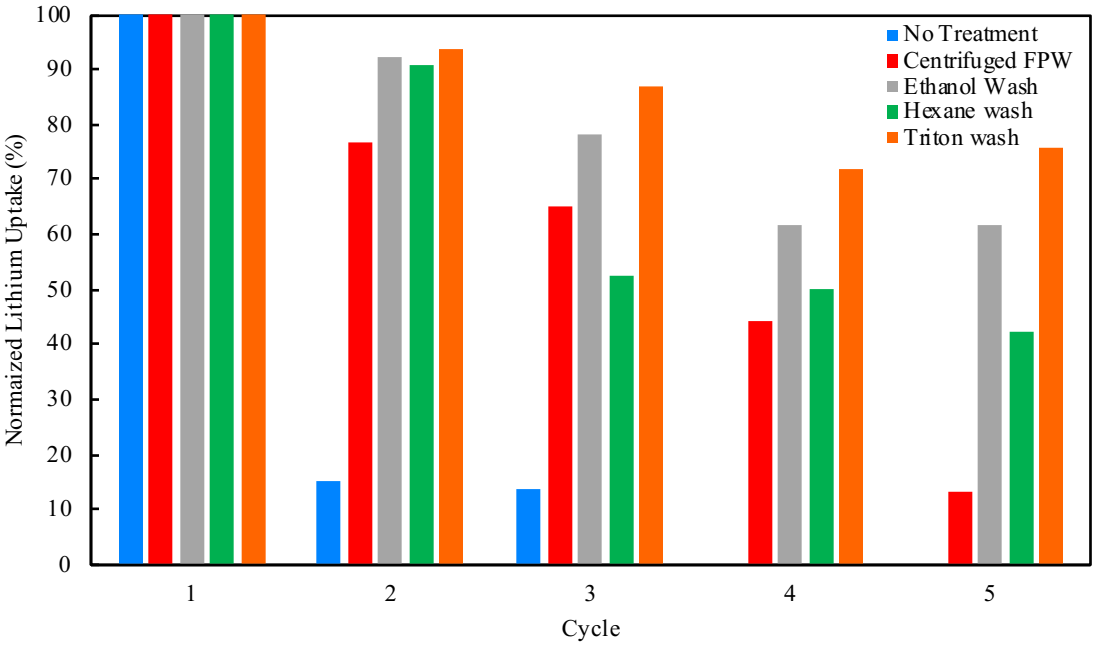

Figure A2: Recycle testing of HMO-2 using various non aqueous organic removal methods. Lithium uptakes are normalized to the first cycle value for each method.

Appendix B: Additional Sorbent Characterization

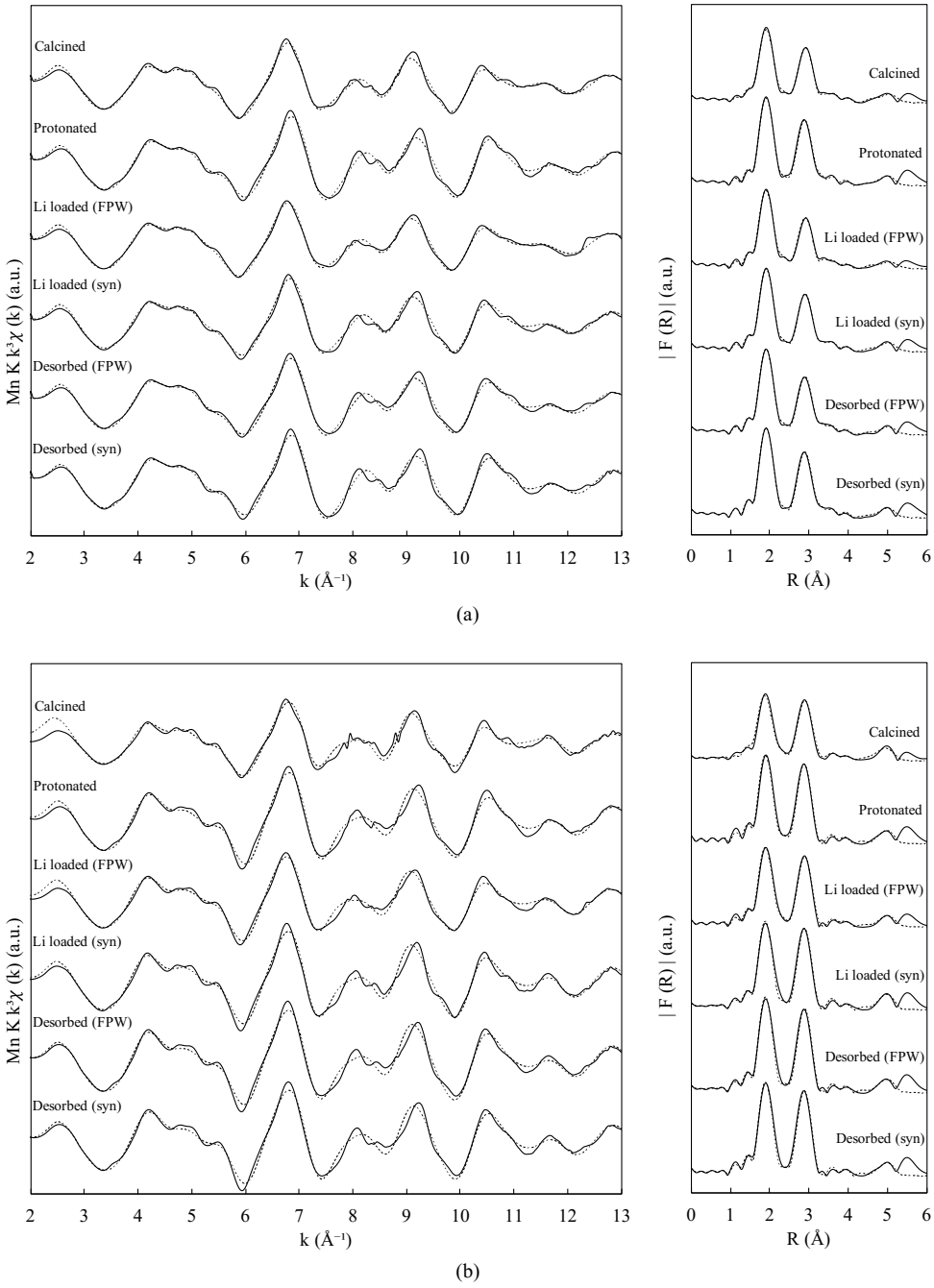

Figure B1: Mn K-edge EXAFS stack plots of LMO/HMO-2 (a) and LMO/HMO-3 (b) after calcination and protonation, as well as after lithium sorption and desorption from synthetic brine and from FPW. LMO/HMO-3 species were fit using a $Li_{1.33}Mn_{1.67}O_4$ model, whereas LMO/HMO-2 species were fit using a 70% $Li_{1.33}Mn_{1.67}O_4$, 30% Mn_2O_3 model; dashed lines represent fits for each material.

Table B1: EXAFS determined 1st shell Mn-O and 2nd shell Mn-Mn distances in LMO/HMO-2 and LMO/HMO-3 after calcination and protonation, as well as after lithium sorption and desorption from synthetic brine and from FPW.

Sorbent	Mn-O		Mn-Mn	
	R (Å)	σ (Å)	R (Å)	σ (Å)
LMO-2 (Calcined)	1.90	0.073	2.90	0.088
HMO-2 (Protonated)	1.90	0.063	2.87	0.083
Li loaded HMO-2 (FPW)	1.90	0.071	2.90	0.092
Li loaded HMO-2 (syn)	1.90	0.068	2.88	0.088
Desorbed HMO-2 (FPW)	1.90	0.066	2.88	0.089
Desorbed HMO-2 (syn)	1.90	0.063	2.87	0.084
LMO-3 (Calcined)	1.89	0.080	2.89	0.087
HMO-3 (Protonated)	1.90	0.063	2.87	0.079
Li loaded HMO-3 (FPW)	1.90	0.069	2.89	0.084
Li loaded HMO-3 (syn)	1.90	0.063	2.88	0.077
Desorbed HMO-3 (FPW)	1.90	0.057	2.88	0.076
Desorbed HMO-3 (syn)	1.90	0.059	2.87	0.075

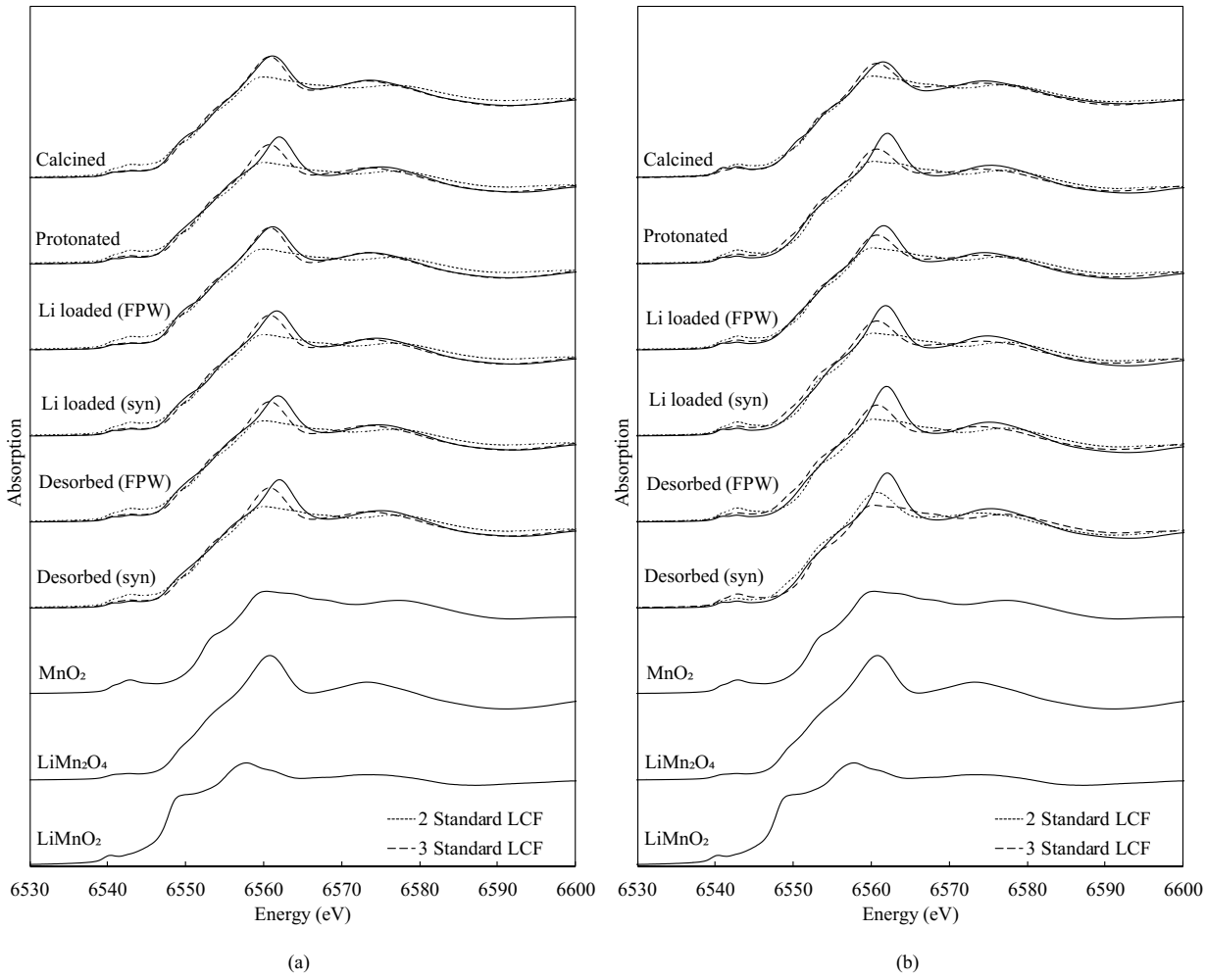

Figure B2: Mn K-edge XANES stack plot of LMO/HMO-2 (a) and LMO/HMO-3 (b) after calcination and protonation, as well as after lithium sorption and desorption from synthetic brine and from FPW. XANES LCFs using 2 reference materials were modelled using MnO_2 and $LiMnO_2$ only; 3 reference material LCFs were modelled using MnO_2, $LiMn_2O_4$ and $LiMnO_2$.

Table B2: Z_{Mn} of sorbent variants derived from XANES linear combination modelling. 2 standard LCFs were modelled using MnO_2 and $LiMnO_2$ only; 3 standard LCFs were modelled using MnO_2, $LiMn_2O_4$ and $LiMnO_2$.

Sorbent	2 Standard Z_{Mn}	3 Standard Z_{Mn}
LMO-2 (Calcined)	3.61	3.56
HMO-2 (Protonated)	3.67	3.61
Li loaded HMO-2 (FPW)	3.60	3.52
Li loaded HMO-2 (syn)	3.67	3.62
Desorbed HMO-2 (FPW)	3.64	3.57
Desorbed HMO-2 (syn)	3.67	3.61
LMO-3 (Calcined)	3.80	3.76
HMO-3 (Protonated)	3.88	3.82
Li loaded HMO-3 (FPW)	3.80	3.72
Li loaded HMO-3 (syn)	3.94	3.90
Desorbed HMO-3 (FPW)	3.90	3.85
Desorbed HMO-3 (syn)	3.91	3.85

Table B3: XPS Mn 3p peak position and Mn 3s multiplet splitting results for all sorbent variants.

Sorbent	Mn 3p position (eV)	Mn 3s Multiplet Split (eV)	Corresponding Mn Surface Valence
LMO-2	49.24	4.71	III, IV
LMO-3	50.11	4.07	IV
HMO-3	49.61	4.38	IV
Li loaded HMO-3 (FPW)	49.74	4.42	IV
Li loaded HMO-3 (syn)	49.84	4.25	IV
Desorbed HMO-3 (FPW)	49.64	4.58	IV
Desorbed HMO-3 (syn)	49.71	4.54	IV

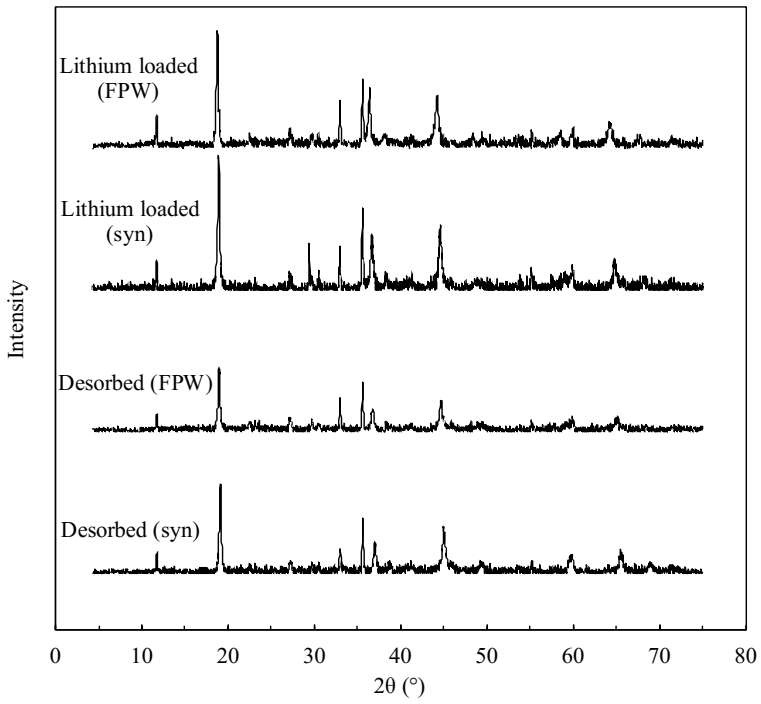

(a)

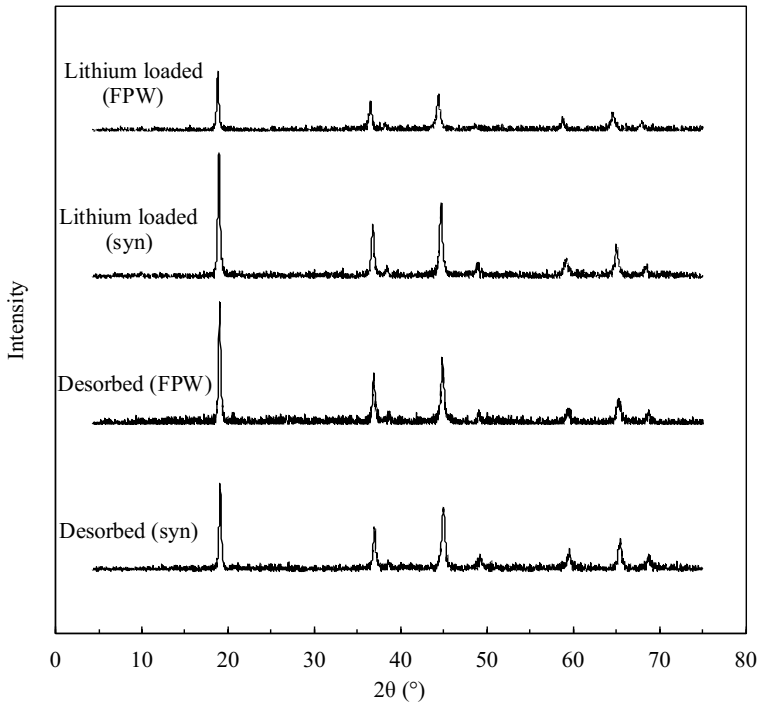

(b)

Figure B3: XRD patterns of lithium loaded and desorbed HMO-2 (a) and HMO-3 (b) from FPW and synthetic brine.

Table B4: BET surface area and pore volume of lithium loaded and desorbed HMO-2 and HMO-3 from FPW and synthetic brine.

Sorbent	BET Surface area ($m^2 g^{-1}$)	Pore Volume ($cm^3 g^{-1}$)
Li loaded HMO-2 (FPW)	33	0.19
Li loaded HMO-2 (syn)	32	0.19
Desorbed HMO-2 (FPW)	75	0.26
Desorbed HMO-2 (syn)	36	0.22
Li loaded HMO-3 (FPW)	70	0.23
Li loaded HMO-3 (syn)	46	0.21
Desorbed HMO-3 (FPW)	71	0.27
Desorbed HMO-3 (syn)	75	0.23